International Journal of *Geo-Information*

MDPI

*Article*

# Impact of Multitemporal Land Use and Land Cover Change on Land Surface Temperature Due to Urbanization in Hefei City, China

**Jing Sun [1] and Suwit Ongsomwang [2,*]**

[1] Department of Geographic Information Science, School of Architectural Engineering, Tongling University, Tongling 244061, China; sunjing@tlu.edu.cn

[2] School of Geoinformatics, Institute of Science, Suranaree University of Technology, Nakhon Ratchasima 30000, Thailand

* Correspondence: suwit@sut.ac.th; Tel.: +66-0898958149

**Abstract:** Land surface temperature (LST) is an essential parameter in the climate system whose dynamics indicate climate change. This study aimed to assess the impact of multitemporal land use and land cover (LULC) change on LST due to urbanization in Hefei City, Anhui Province, China. The research methodology consisted of four main components: Landsat data collection and preparation; multitemporal LULC classification; time-series LST dataset reconstruction; and impact of multitemporal LULC change on LST. The results revealed that urban and built-up land continuously increased from 2.05% in 2001 to 13.25% in 2020. Regarding the impact of LULC change on LST, the spatial analysis demonstrated that the LST difference between urban and non-urban areas had been 1.52 K, 3.38 K, 2.88 K and 3.57 K in 2001, 2006, 2014 and 2020, respectively. Meanwhile, according to decomposition analysis, regarding the influence of LULC change on LST, the urban and built-up land had an intra-annual amplitude of 20.42 K higher than other types. Thus, it can be reconfirmed that land use and land cover changes due to urbanization in Hefei City impact the land surface temperature.

**Keywords:** multitemporal land use and land cover classification; land surface temperature; single-channel; harmonic analysis; Landsat; Hefei City; China



**Citation:** Sun, J.; Ongsomwang, S. Impact of Multitemporal Land Use and Land Cover Change on Land Surface Temperature Due to Urbanization in Hefei City, China. *ISPRS Int. J. Geo-Inf.* **2021**, *10*, 809. https://doi.org/10.3390/ijgi10120809

Academic Editor: Wolfgang Kainz

Received: 11 August 2021
Accepted: 27 November 2021
Published: 30 November 2021



## 1. Introduction

Land surface temperature (LST) is an essential parameter in the climate system, and its dynamics can be used to indicate climate change [1–8]. Generally, LST is regularly measured from a thermal infrared (TIR) band of satellite sensors, such as Landsat (moderately spatial resolution) and MODIS (high temporal resolution). Additionally, the derived LST data from the TIR bands of a satellite are crucial to understanding the impacts of urbanization on account of land use and land cover (LULC) change [9]. LST is a quantity concerning the surface of the Earth, which is highly variable in space and time. The temporal variability mainly comes from the annual and daily cyclical changes in solar radiation and is further affected by weather conditions, while the spatial variability is impacted by surface characteristics, such as albedo, emissivity, soil moisture, and topography [10–15].

Moreover, the estimated satellite LST, as primary input data, has been applied to determine the near-ground air temperature in various studies, such as urban heat island mapping and its intensity analysis due to urbanization [16–34].

Nevertheless, all the mentioned LST-related research only focuses on the analysis of a single satellite scene. Many researchers can choose only one satellite scene from one year to estimate LST data due to cloud coverage. The interference of clouds is a critical issue in satellite derived LST data. Xu and Shen [35] stated that LST cannot be retrieved from remote sensing images that are covered by clouds, and the lack of LST information caused by cloud coverage limits the application of remote sensing LST data.

Moreover, the temporal analysis of the thermal landscape needs to consider the thermal characteristics that change over time. Non-stationary modeling of the temporal thermal landscape can be avoided by dividing time-series observations into different segments corresponding to different LULC types [9]. Therefore, it is valuable and necessary to use the time-series LST dataset to reveal the urban thermal dynamics resulting from land cover transformation [36]. Unfortunately, time-series LST datasets at a medium spatial resolution, i.e., Landsat, with regular temporal frequency, are not readily available for public service.

Many studies have been conducted to reconstruct time-series LST data from satellite sensors with various approaches to minimize the effect of cloud cover in recent years. Nonetheless, most of the studies focused on low spatial and high temporal resolutions. For example, Neteler [37] reconstructed daily MODIS LST data in the central–eastern area of the Alps based on the temperature gradient using all available daily LST data during 2000 and 2008. Ke et al. [38] used the regression kriging method to reconstruct the 1462 eight-day MODIS LST data in the central Qinghai–Tibet Plateau. Xu and Shen [35] applied the harmonic analysis (HA) algorithm to remove cloud-affected observations and reconstructed 8-day LST for MODIS LST data in 2005 over the Yangtze River Delta region in China. Kang et al. [39] reconstructed daily MODIS LST data in 2014 based on the spatiotemporal autocorrelation of land surface variables for the Babao River Basin of the Tibetan Plateau in Northwestern China. Therefore, the HA model has become one of the most widely used models to fit time-series data, because it can identify and remove contaminated pixels [8,40] and simulate time-series curves through temporal dimensional interpolation with fewer available input data [41]; thus, it is here proposed to reconstruct time-series Landsat LST data.

In this study, the reconstruction of time-series LST with multitemporal LULC datasets will be developed to correct the existing error of LST due to contaminated pixels and overestimated LST values under the MATLAB environment. In practice, a spatiotemporal indicator cube (correct and incorrect pixels) will be constructed using a reshape function by converting space to time in order to indicate which pixel's LST values need to be correct. Then, the incorrect LST values are replaced with new LST values using the HA model, whereas the correct LST values remain; thereby, a time-series LST dataset can be reconstructed using a reshape function by converting time to space. Using spatial and decomposition analyses, the derived time-series LST data will be further applied to examine the impact of LULC change on LST in Hefei City due to rapid urbanization between 2001 and 2020. In the study, all available Landsat 5/7/8 scenes over the city in this period were downloaded to classify LULC dataset using harmonic analysis with a minimum spectral distance algorithm [42], estimate time-series LST using the single-channel method, reconstruct time-series LST using a harmonic analysis model, and examine the impact of LULC change on LST.

The objectives of this study were (1) to classify multitemporal LULC maps using harmonic analysis with a minimum spectral distance algorithm, (2) to estimate time-series LST data using a single-channel algorithm, (3) to reconstruct time-series LST data using a harmonic analysis model, and (4) to examine the impact of LULC change on LST using spatial analysis and decomposition analysis. Ultimately, the adopted and developed methods were applied to classify LULC datasets in 2001, 2006, 2014, and 2020, and to assess the status and changes that directly impact the land surface temperature in the spatial and time domain in Hefei City, Anhui Province, China.

## 2. Materials and Methods

### *2.1. Study Area*

Hefei City is the capital city of Anhui Province, China, and the largest city of this province as well, comprising four urban districts (Shushan, Luyang, Yaohai, and Baohe), one county-level city (Chaohu), and four counties (Changfeng, Feidong, Feixi, and Lujiang). Hefei City covers an area of 11,465 km$^2$ and is situated between 116°30′–118°00′ E and

30°30′–33°00′ N. Hefei has a north subtropical monsoon climate with four distinct seasons. Its winter and summer are long, but spring and autumn are shorter. The winter is cold and dry, the summer is hot, while the spring and autumn are wet and warm. It is situated between the Yangtze River and the Huai River and is dominated by plains and hills. The city's altitude is mostly between 15 and 80 meters, with the highest altitude of 595 meters. The terrain of the main urban area slopes from the northwest to the southeast. Chaohu Lake, one of China's five largest freshwater lakes, is 55 kilometers long from east to west and 21 kilometers wide from north to south. It has a water area of approximately 770 km$^2$ and is situated southeast of the study area (Figure 1). In addition, in Figure 1, Point_U, Point_A, Point_F, and Point_W are four points taken from the old town, rice fields, forest parks and Chaohu Lake, representing the four LULC types of urban and built-up land, agricultural land, forest land and water bodies, respectively. Moreover, the LULC types at these four points have not changed during 2001–2020. Furthermore, Point_AU is taken from Hefei Xinqiao International Airport, in the northwest of Hefei City, and its LULC type has changed from agricultural land to urban and built-up land around 2010.

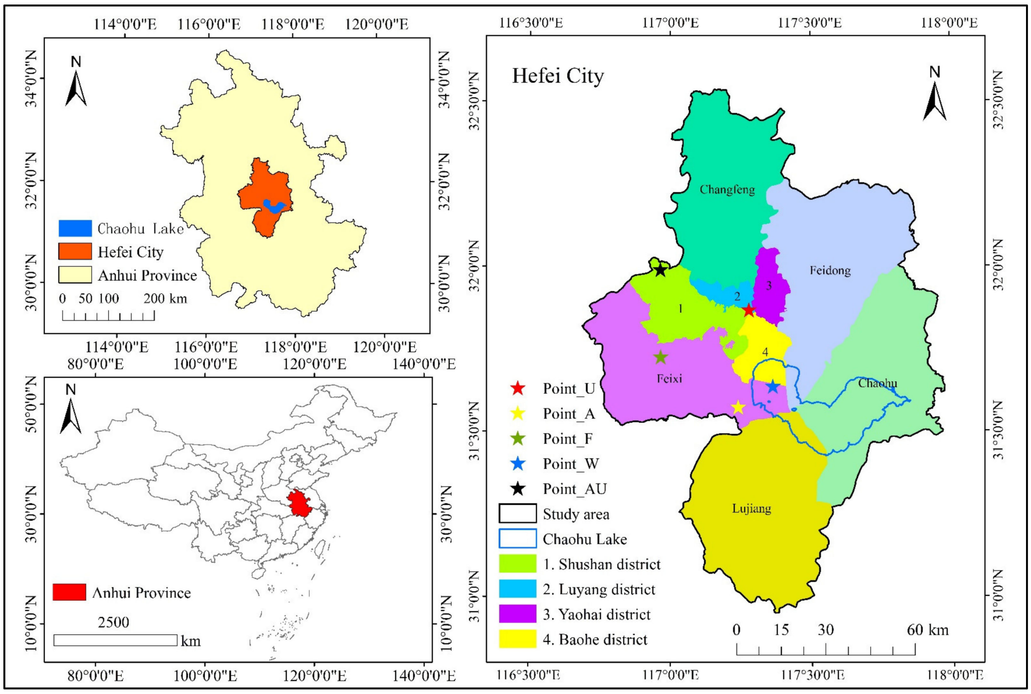


**Figure 1.** Location map of the study area.

Meanwhile, the rapid social and economic development of Hefei City has driven the expansion of the city, led to the transformation of natural land cover and changes in the biophysical environment, and changed the surface energy process [43]. According to reports released by the Statistics Bureau of Anhui Province [44] in 2020, the urban population of Hefei City increased from 1.38 million persons in 2001 to 2.91 million persons in 2019, and this phenomenon led to LULC change in the city: built-up areas increased from 125 km$^2$ in 2001 to 481 km$^2$ in 2019 (Table 1). These statistics indicate the rapid urbanization of Hefei City between 2001 and 2019. As a result, the scope of selection data in this study is focused on this period. Therefore, available time-series Landsat datasets between 2001 and 2020 were collected to assess the impact of multitemporal LULC change on LST due to urbanization in Hefei City.

**Table 1.** Urban population and built-up areas of urban districts of Hefei City from 2001 to 2019 *.

| Year | Urban Population (Million) | Built-Up Areas ($km^2$) |
|---|---|---|
| 2001 | 1.38 | 125 |
| 2002 | 1.47 | 148 |
| 2003 | 1.56 | 148 |
| 2004 | 1.64 | 148 |
| 2005 | 1.75 | 225 |
| 2006 | 1.93 | 225 |
| 2007 | 1.98 | 225 |
| 2008 | 2.03 | 280 |
| 2009 | 2.09 | 280 |
| 2010 | 2.16 | 326 |
| 2011 | 2.18 | 360 |
| 2012 | 2.22 | 378 |
| 2013 | 2.41 | 393 |
| 2014 | 2.45 | 403 |
| 2015 | 2.51 | 416 |
| 2016 | 2.59 | 460 |
| 2017 | 2.70 | 461 |
| 2018 | 2.81 | 466 |
| 2019 | 2.91 | 481 |

* The statistics data from Statistics Bureau of Anhui Province only include four urban districts.

### 2.2. Datasets

Due to the limitation of cloud cover, the available Landsat images with cloud cover of less than 90% were used in this study [45]. Therefore, a series of a total of 552 scenes (Level-1 products, path 121/row 38) between 1 January 2001 and 31 December 2020 were downloaded via the USGS website (https://earthexplorer.usgs.gov/) (accessed on 25 February 2021). Among them, 145 images were from Landsat 5, 289 images were from Landsat 7, and 118 images were from Landsat 8, and the distribution of these images is shown in Figure 2.

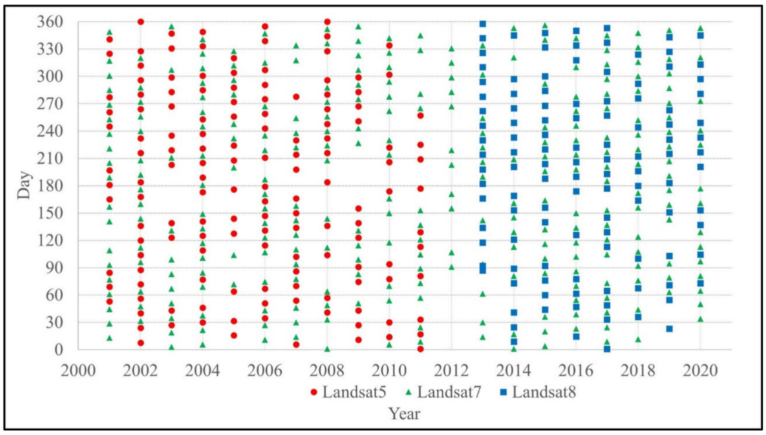


**Figure 2.** The distribution of available Landsat 5, 7, and 8 imageries from January 2001 to December 2020.

The MODIS water vapor data (MOD05_L2 collection 6.1 products) of MODIS/Terra with the same date as a selection of Landsat data were downloaded from the LAADS DAAC website (https://ladsweb.modaps.eosdis.nasa.gov/) (accessed on 25 February 2021).

### 2.3. Research Methodology

The research methodology comprised four components: (1) Landsat data collection and preparation, (2) multitemporal LULC classification, (3) time-series LST dataset reconstruction and verification, and (4) impact of multitemporal LULC change on LST. The workflow and connections between each component are presented in Figure 3.

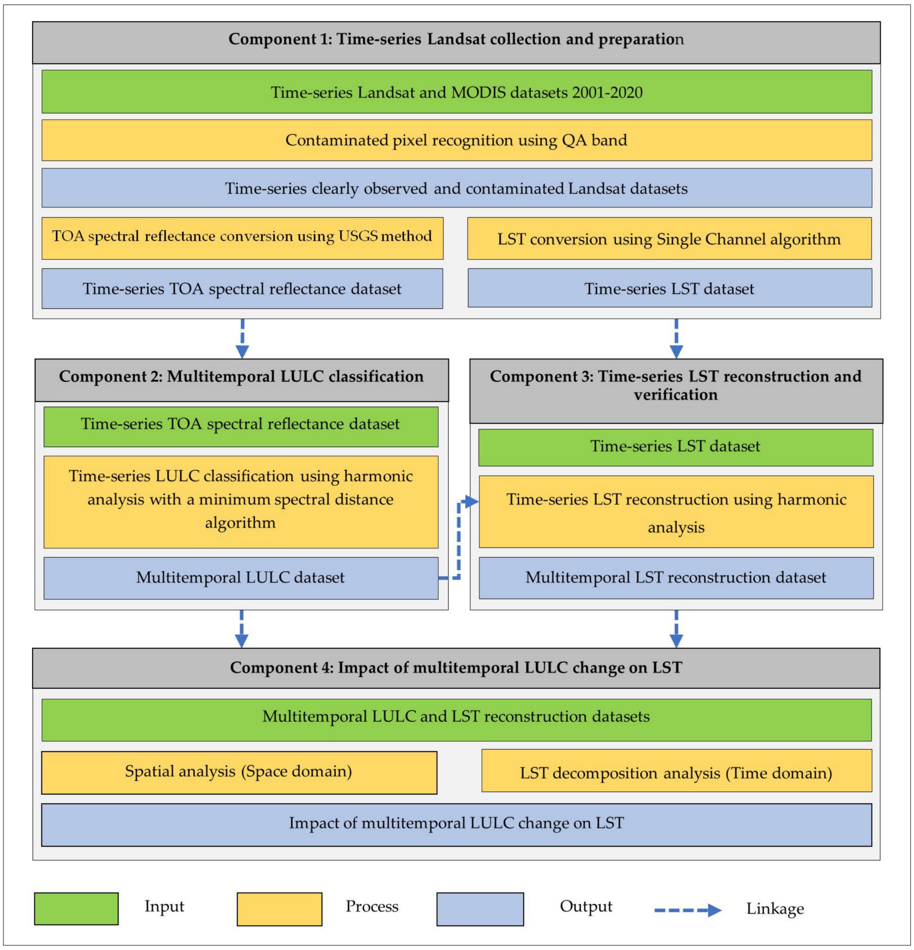


**Figure 3.** Workflow and connections of research methodology components.

### 2.3.1. Landsat data collection and preparation

All downloaded time-series Landsat datasets between 2001 and 2020, with 552 scenes, were prepared in four separate steps according to four significant processes of this component: contaminated pixel recognition, contaminated pixel assessment, TOA spectral reflectance conversion, and time-series LST conversion and water vapor content depth extraction. The details of each step are described in the following sections.

(1) Contaminated pixel recognition

Each pixel in the quality assessment (QA) band of Landsat 5, 7, and 8 products comprises information associated with the terrain, radiometric saturation, cloud, and cloud shadow. In this step, Landsat QA tools [46] with per-pixel filtering techniques were applied to identify the coverage of contaminated pixels. The percentage of coverage of contaminated pixels was calculated based on the number of contaminated pixels of each scene and the number of pixels in the study area (Hefei City). If the contaminated pixel's coverage of an image in the study area was greater than 50%, it was removed prior to data analysis.

(2) Contaminated pixel assessment

In this step, the percentage of the total clearly observed pixels (non-contaminated pixels) and the percentage of total images by percentage of contaminated pixels were first extracted to reduce the number of scenes and costs, and the higher percentage of the clearly observed total pixels was used for the data analysis. Then, the percentage of total images and total clearly observed pixels, according to 10 interval classes (≤10, ≤20, . . . , ≤100), of the percentage of contaminated pixels (%), was calculated using Equations (1) and (2):

$$P_{image,i} = \frac{N_{image,i}}{N} * 100\% \tag{1}$$

$$P_{pixel,i} = \frac{\sum_0^j N_j * (1-j) * M}{N * M} * 100\% \tag{2}$$

where $P_{image,i}$, $P_{pixel,i}$, and $N_{image,i}$ are the percentage of total images, percentage of total clearly observed pixels, and number of images, respectively, where $i$ is the percentage of contaminated pixels (≤10%, ≤20%, . . . ≤100%), and $N$ is the number of total images ($N$ = 552 in this study). $j$ is the percentage of contaminated pixels (%), $N_j$ is the number of images when the percentage of contaminated pixels (%) is $j$, and $M$ is the number of pixels in the image.

(3) TOA spectral reflectance conversion

Radiometric correction (e.g., sensor calibration, atmospheric correction, terrain correction, and relative radiation normalization) is essential to guarantee the homogeneity of the time-series data for change detection [47]. The Landsat Ecosystem Interference Adaptive Processing System (LEDAPS) and the Landsat 8 Surface Reflection Code (LaSRC) are used to convert Landsat TM/ETM and OLI level-1 data to surface reflectance Landsat Surface Reflectance Higher-Level Data Products [48,49].

The TOA spectral reflectance was converted from Landsat Level-1 products using Equation (3) as suggested by USGS [48,49].

$$\rho\lambda' = M_\rho * Q_{cal} + A_\rho \tag{3}$$

where $\rho\lambda'$ is the TOA spectral reflectance, $Q_{cal}$ is the digital number value, and $M_\rho$ and $A_\rho$ are the reflectance multiplicative scaling factor and additive scaling factor, respectively.

(4) Time-series LST conversion and water vapor content depth extraction

For time-series LST conversion, the single-channel (SC) algorithm that was developed by [50,51] was applied to calculate LST using Equations (4) to (6).

$$T_s = \gamma \left[ \frac{1}{\varepsilon} (\varphi_1 L_{sen} + \varphi_2) + \varphi_3 \right] + \delta \tag{4}$$

$$\gamma \approx \frac{T_{sen}^2}{b_\gamma L_{sen}} \tag{5}$$

$$\delta \approx T_{sen} - \frac{T_{sen}^2}{b_\gamma} \tag{6}$$

where $T_s$ is the land surface temperature, $\varepsilon$ is the surface emissivity, $\gamma$ and $\delta$ are two parameters, and $T_{sen}$ is the at-sensor brightness temperature (BT); $b_\gamma$ are 1256 K, 1277 K, and 1324 K for Landsat 5 band 6, Landsat 7 band 6, and Landsat 8 band 10, respectively, and $\varphi_1$, $\varphi_2$, and $\varphi_3$ are the atmospheric functions.

The practical approach proposed in the SC method includes the approximation of the atmospheric functions defined in Equation (7) versus the atmospheric water vapor content from a second-order polynomial fit, expressed in matrix notation as follows:

$$\begin{bmatrix} \varphi_1 \\ \varphi_2 \\ \varphi_3 \end{bmatrix} = \begin{bmatrix} c_{11} & c_{12} & c_{13} \\ c_{21} & c_{22} & c_{23} \\ c_{31} & c_{32} & c_{33} \end{bmatrix} \begin{bmatrix} w^2 \\ w \\ 1 \end{bmatrix} \tag{7}$$

where the coefficients $c_{ij}$ are obtained by simulation, $w$ is the atmospheric water vapor content.

In practice, the atmospheric functions $\varphi_1$, $\varphi_2$, and $\varphi_3$ for band 6 of Landsat 5/7 and band 10 of Landsat 8 can be obtained from Equations (8) and (9) suggested by [50,51].

$$\begin{bmatrix} \varphi_1 \\ \varphi_2 \\ \varphi_3 \end{bmatrix} = \begin{bmatrix} 0.14714 & -0.15583 & 1.1234 \\ -1.1836 & -0.37607 & -0.52894 \\ 0.04554 & 1.8719 & -0.39071 \end{bmatrix} \begin{bmatrix} w^2 \\ w \\ 1 \end{bmatrix} \tag{8}$$

$$\begin{bmatrix} \varphi_1 \\ \varphi_2 \\ \varphi_3 \end{bmatrix} = \begin{bmatrix} 0.04019 & 0.02916 & 1.01523 \\ -0.38333 & -1.50294 & 0.20324 \\ 0.00918 & 1.36072 & -0.27514 \end{bmatrix} \begin{bmatrix} w^2 \\ w \\ 1 \end{bmatrix} \tag{9}$$

Meanwhile, the required BT for LST calculation was calculated in two steps: converting digital numbers of the TIR band to spectral radiance using Equation (10) and converting spectral radiance to BT using Equation (11).

$$L_\lambda = M_L * Q_{cal} + A_L \tag{10}$$

$$BT = K_2 / \ln(K_1/L_\lambda + 1) \tag{11}$$

where $L_\lambda$ is the spectral radiance (W/ (m$^2$·sr·µm)), $Q_{cal}$ is the digital number value, and $M_L$ and $A_\lambda$ are the radiance multiplicative scaling factor and additive scaling factor, respectively. BT is the brightness temperature in Kelvin (K); $K_1$, and $K_2$ are the thermal conversion constants.

For emissivity extraction, since the emissivity changes with the wavelength, the normalized difference vegetation index (NDVI) threshold method developed by [52] is widely used for emissivity calculation. Here, the NDVI threshold method is improved by introducing the normalized difference water index (NDWI) to quickly identify the water bodies and produce a uniform emissivity value because the emissivity of water bodies is quite stable in comparison with non-water bodies. Finally, Equations (12) and (13) are applied to calculate the emissivity of different land surfaces.

$$\varepsilon_\lambda = \begin{cases} \varepsilon_{w\lambda} & NDWI > 0 \\ \varepsilon_{s\lambda} & NDWI \leq 0 \; and \; 0 < NDVI < NDVI_s \\ \varepsilon_{v\lambda} \cdot P_v + \varepsilon_{s\lambda} \cdot (1 - P_v) + C_\lambda & NDWI \leq 0 \; and \; NDVI_s \leq NDVI \leq NDVI_v \\ \varepsilon_{v\lambda} \cdot P_v + C_\lambda & NDWI \leq 0 \; and \; NDVI > NDVI_v \end{cases} \tag{12}$$

$$C_\lambda = (1 - \varepsilon_{s\lambda}) \cdot \varepsilon_{v\lambda} \times F' \cdot (1 - P_v) \tag{13}$$

where $\varepsilon_\lambda$ is the band emissivity, $\varepsilon_{v\lambda}$, $\varepsilon_{s\lambda}$, and $\varepsilon_{w\lambda}$ are the emissivity of vegetation, soil, and water bodies, respectively, $P_v$ is the proportion of vegetation, $C_\lambda$ is a coefficient related to surface roughness ($C$ = 0 for a flat surface), $NDVI_v$ and $NDVI_s$ are the $NDVI$ for a fully vegetated pixel and a fully soil pixel, respectively, and $F'$ is a geometrical factor ranging between zero and one, $F'$ = 0.5 is generally chosen, as suggested by [52].

The proportion of vegetation was estimated as follows [53]:

$$P_v = \left( \frac{NDVI - NDVI_s}{NDVI_v - NDVI_s} \right)^2 \tag{14}$$

In this study, the values of $NDVI_v$ and $NDVI_s$ are 0.5 and 0.2, respectively, as suggested by [52].

The average emissivity of representative materials was calculated based on the spectral response function of the thermal infrared (TIR) band of Landsat using the ASTER spectral database [54] with Equation (15), suggested by [55], as shown in Table 2.

$$X = \frac{\int_{\lambda_1}^{\lambda_2} f(\lambda) X(\lambda) d\lambda}{\int_{\lambda_1}^{\lambda_2} f(\lambda) d\lambda} \tag{15}$$

where $X$ is the average emissivity in the thermal infrared band of Landsat, $X(\lambda)$ is various spectral quantities considered as emissivity, $\lambda_1$ and $\lambda_2$ are the lower and upper boundaries of the wavelength in the TIR band of Landsat, and $f(\lambda)$ is the spectral response function.

**Table 2.** The emissivity of representative materials in Landsat TIR bands.

| TIR Bands | Wavelength (µm) | Emissivity | | |
|---|---|---|---|---|
| | | Water Bodies | Soil | Vegetation |
| Band 6 of Landsat 5 | 10.40–12.50 | 0.9887 | 0.9724 | 0.9834 |
| Band 6 of Landsat 7 | 10.40–12.50 | 0.9892 | 0.9712 | 0.9828 |
| Band 10 of Landsat 10 | 10.60–11.19 | 0.9908 | 0.9695 | 0.9817 |

The water vapor content is an essential parameter for LST conversion using the SC algorithm since Landsat itself does not have a band that can detect water vapor content depth; as an alternative, the MODIS water vapor data was used in this study because the time of MODIS/Terra obtaining the data during the day is very close to the time when Landsat acquires the data. The digital number values were divided by the scaling factor (1000) to extract the vertical column of water vapor content depth in cm [56].

#### 2.3.2. Multitemporal LULC Classification

Multitemporal LULC datasets, which included urban and built-up land (U), agricultural land (A), forest land (F), and water bodies (W), were classified using the method developed by Sun and Ongsomwang [42]. In practice, the clearly observed and identified contaminated pixels (with value 0 or 1) from all selected scenes were firstly applied to construct a spatiotemporal cube. Similarly, six spatiotemporal cubes were created from six spectral reflectance bands (with values 0 to 1). Then, two time-dimension datasets, which were obtained through reading pixel by pixel from the cubes, were combined to remove the contaminated pixels for the time-series spectral reflectance reconstruction (see Figure 4).

The spectral reflectance data were further used for multi-temporal LULC classification using the following steps.

(1) Stable pixels of the LULC type extraction. Four LULC maps (2001, 2006, 2014, and 2020) classified using the maximum likelihood classifier algorithm were simultaneously superimposed to identify the common area of each LULC type from four different years. The derived results show the stable pixels for each LULC category from 2001 to 2020.

(2) Harmonic function curve transformation and standard harmonic curve construction. The sample points from four stable LULC types were randomly selected and transformed into harmonic function curves. These curves were further used to construct standard harmonic curves for the six spectral bands.

(3) Spectral distance measurement and probability calculation. The normalized spectral distance between the standard harmonic function curve of each LULC type and an unclassified pixel at the same specific time point was calculated. Then, the normalized spectral distance of an unclassified pixel to any LULC type was applied to calculate the probability of an unclassified pixel being a specific LULC type.

(4) Multitemporal LULC classification. The average probabilities of an unclassified pixel being a specific LULC type (U, A, F, and W) from among the six spectral bands (blue, green, red, NIR, SWIR1, and SWIR2) were calculated and compared to identify the

highest value; the corresponding LULC type that provided the highest probability was then assigned to an unclassified pixel at a specific time point. For further details, see Sun and Ongsomwang [42].

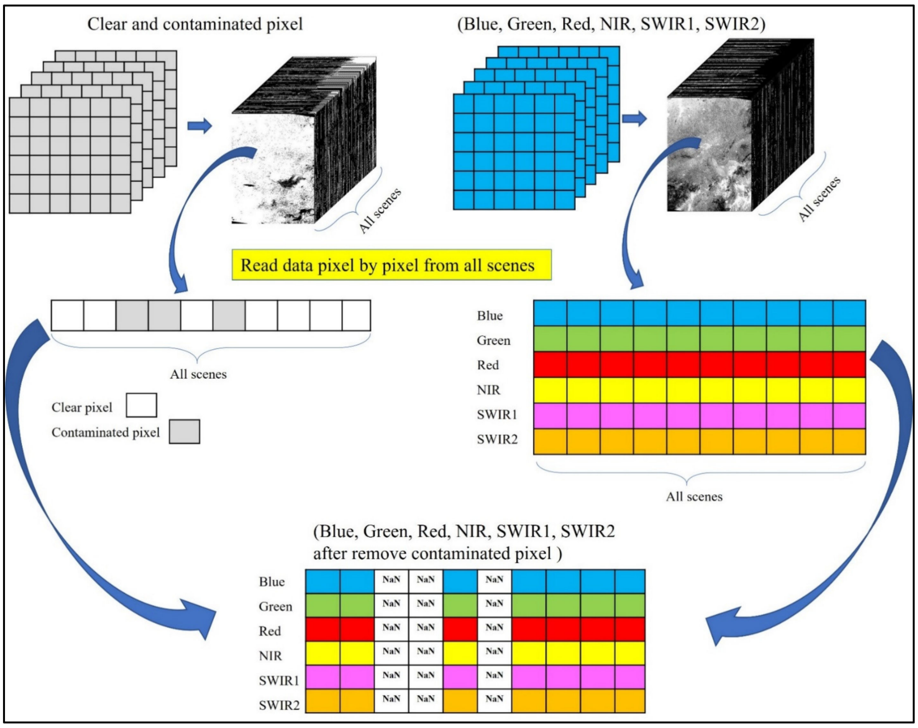


**Figure 4.** Time-series spectral reflectance reconstruction.

In addition, producer's accuracy (PA), users' accuracy (UA), overall accuracy (OA), and Kappa hat coefficient were assessed based on the error matrix between classified multitemporal LULC data and ground reference information from Landsat data themselves [57]. The number of samples for thematic accuracy assessment was calculated based on Equation (16), suggested by [57,58]. The allocation of sample points could be realized by utilizing a stratified random sampling technique. In practice, reference information of each sample point was visually interpreted using the elements (e.g., color, size, shape, shadow, and texture) of image interpretation [59] and compared with the classified LULC type to construct an error matrix for thematic accuracy assessment.

$$N = \frac{B\Pi_i(1-\Pi_i)}{{b_i}^2} \tag{16}$$

where $\Pi_i$ is the portion of a population in the $i$th class out of $k$ classes that has the proportion closest to 50%, $b_i$ is the desired precision (e.g., 5%) for the class, $B$ is the upper $(\alpha/k) \times 100$ percentile of the Chi-square distribution with 1 degree of freedom, and $k$ is the number of classes.

2.3.3. Time-Series LST Reconstruction and Verification

As mentioned previously, LST-related research frequently focuses on the analysis of a single scene. Therefore, the HA model with multitemporal spatiotemporal cubes was applied to reconstruct time-series LST in order to minimize error. Under this component, four separate steps, including the construction of an indicator cube for LST correction, simulation of LST using the HA model, time-series LST reconstruction, and verification of the LST dataset, are implemented (Figure 5), as follows:

(1) Construction of indicator cube for LST correction

The indicator cubes, including the data and algorithm cube, were separately constructed using a reshape function by converting space to time in order to determine the correctness of LST estimation by the SC algorithm. In this step, the data cube (LST estimated from clear or contaminated pixels) and algorithm cube (water vapor content depth is higher than or lower than 3 $g/cm^2$) were first separately prepared using the reshape function by converting space to time. Then, they were multiplied to construct an indicator cube for LST correction.

For data cube preparation, the time-series LST values calculated using the SC algorithm from clearly observed pixels were considered correct LST values. In contrast, LST values calculated using the SC algorithm from contaminated pixels were considered incorrect LST values. Thus, the values of the data cube consisted of 0 (incorrect LST) and 1 (correct LST).

For algorithm cube preparation, the time-series water vapor content depth dataset of MODIS was classified into two groups using the threshold value of 3 $g/cm^2$ to indicate the correctness of the algorithm, as suggested by [50,51]. If time-series LST values were calculated from pixels with a water vapor content depth of less than or equal to 3 $g/cm^2$, they were considered correct time-series LST values. If time-series LST values were calculated from pixels with a water vapor content depth higher than 3 $g/cm^2$, they were considered incorrect LST values. Therefore, the values of the algorithm cube included 0 (incorrect LST according to water vapor content depth) and 1 (correct LST according to water vapor content depth).

Subsequently, the data cube and algorithm were combined to construct the indicator cube, with a value of 0 and 1, using a multiplicative operation for time-series LST correction.

(2) Simulation of LST using the HA model

To obtain the characteristics of time-series LST values, the selected estimated LST from clearly observed pixels between 2001 and 2020 was converted into a spectral harmonic curve with an HA model by applying Equation (16), modified from Zhu and Woodcock [9].

$$y = a + bt + A\,cos\left(\frac{2\pi}{T}t - \varphi\right) \tag{17}$$

where $t$ is the Julian date, $y$ is the reconstructed LST value at the Julian date $t$, $T$= 365, $a$, $b$, $A$, and $\varphi$ are values of the intercept, slope, amplitude, and phase, respectively.

In this step, the estimated LST cube, the indicator cube with the value of 0 or 1, and the LULC cube, with a value of LULC type 1, 2, 3, or 4 (i.e., 1 is urban and built-up land, 2 is agricultural land, 3 is forest land, and 4 is water bodies) were used to calculate the simulated LST using the HA model. The time-series estimated LST of each location was first divided into a LULC time-series homogeneous segment; then, harmonic terms could be calculated from the correct LST (value of indicator cube = 1), in which the harmonic terms were constant in each segment. Accordingly, the simulated time-series LST values could be recalculated at any time according to the harmonic terms.

(3) Time-series LST reconstruction

The estimated LST cube and simulated LST cube were simultaneously applied to construct time-series LST between 2001 and 2020 according to the indicator cube, as follows:

If the LST indicator cube showed that the estimated LST values were correct, the reconstructed LST values were taken from the estimated LST dataset.

If the LST indicator showed that the estimated LST values were incorrect, reconstructed LST values were taken from the simulated LST dataset.

Based on this approach, a new LST cube was first reconstructed and then reshaped from time to space to create a time-series LST dataset.

(4) Verification of LST dataset

As mentioned in the previous section, the reconstructed time-series LST values came from two parts: one came from the time-series estimated LST using the SC algorithm, and the other came from the simulated time-series LST value based on HA recalculation. Subsequently, the estimated time-series LST values using the SC algorithm with clear pixels and a depth of water vapor content less than or equal to 3 $g/cm^2$ were acceptable, as suggested by [50,51]. On the contrary, the simulated time-series LST values with contaminated pixels or a depth of water vapor content higher than 3 $g/cm^2$ were required in order to verify whether the calculated values were consistent with the actual ground temperature values. However, it is difficult to obtain the precise ground temperature of this part in actual operation due to the atmospheric influence (cloud, water vapor) and other conditions, making it difficult to verify the accuracy of this simulated value directly.

Accordingly, as an alternative, the simulated time-series LST data using the HA model were compared with correct estimated time-series LST using the SC algorithm for the verification of the dataset using the mean error (*ME*) and mean absolute error (*MAE*), as suggested by [60,61], as:

$$ME = \frac{\sum_{i=1}^{n}(y_i - x_i)}{n} \tag{18}$$

$$MAE = \frac{\sum_{i=1}^{n}|y_i - x_i|}{n} \tag{19}$$

where $x_i$ is the correct estimated LST value, $y_i$ is the corresponding simulated LST value, and $n$ is the total number of correct LST pixels of all scenes.

### 2.3.4. Impact of multitemporal LULC change on LST

In this study, the impact of multitemporal LULC change on LST was examined with two approaches, including the time domain using decomposition analysis and the spatial domain using spatial analysis.

(1) Spatial analysis and impact of LULC change on LST

The impact of LULC change on LST was assessed using zonal statistics analysis based on the derived LST and multitemporal LULC data in 2001, 2006, 2014, and 2020. The area and mean LST of urban and non-urban areas of Hefei City and their subordinate districts/counties/county-level city in 2001, 2006, 2014, and 2020 were counted, respectively. Furthermore, we evaluated the LST difference between urban and non-urban areas in different regions in different years and the LST difference in urban areas at different scales.

(2) Decomposition analysis and impact of LULC change on LST

The reconstructed LST was first decomposed into three parts—trend component (intercept and slope), seasonality component (amplitude and phase), and residual component—according to each pixel's LULC type. Equations that were modified from Fu and Weng [45] were applied to calculate these components as follows:

$$Y_t = T_t + S_t + \varepsilon_t \tag{20}$$

$$T_t = a + bt \tag{21}$$

$$S_t = A\ cos\left(\frac{2\pi}{T}t - \varphi\right) \tag{22}$$

where $t$ is the Julian date, $Y_t$ is the time-series observation, $T_t$ is the trend component, $S_t$ is the seasonality component, and $\varepsilon_t$ is the noise. $a$ and $b$ are the linear trend coefficients, $A$ and $\varphi$ are the periodic coefficients, $T$ = 365.

Next, the impact of LULC change on LST was evaluated based on the derived harmonic terms of LST from a 20-year period. In this study, three aspects, including (1) harmonic terms of average LST values of different LULC types; (2) the distribution of harmonic terms of LST of different LULC types; and (3) the impact of LULC change on harmonic terms of LST, were investigated.

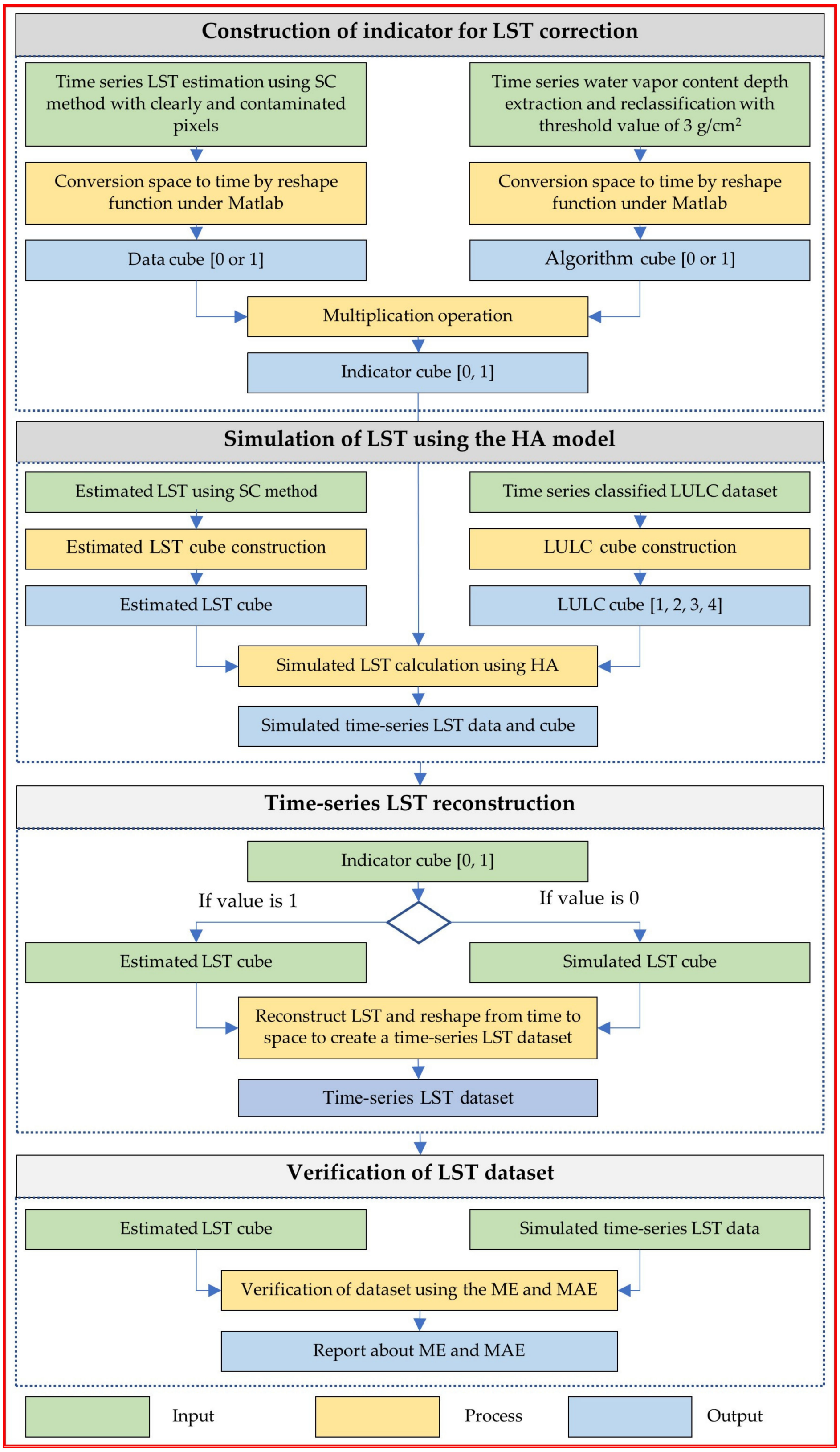


**Figure 5.** Workflow for time-series LST reconstruction and verification.

Firstly, the average LST values of four different LULC types were calculated for all selected scenes from 2001 to 2020. Meanwhile, the four groups of LST values were plotted as curves. Then, the HA was used to fit these groups of curves in order to obtain harmonic terms (intercept, slope, amplitude, and phase) for comparison of the intra-annual and inter-annual LST changes of different LULC types.

In addition, the values of the harmonic term of LST of each LULC type were also counted based on the time-series LULC data. Then, the frequency of each harmonic term of each LULC type was plotted as a histogram distribution to compare each harmonic term value. Since the sample size and bin width of the histogram from different LULC types are different, it is difficult to compare them. Herein, the normalized histogram was presented. Moreover, the average value of the harmonic term of the LST of each LULC type was also extracted and compared to their values.

Furthermore, the pixels with the LULC change from possible changes (e.g., A to U, F to U, W to U, etc.) were selected under HA. The harmonic term values of the LST of these selected pixels before and after the LULC change were extracted, and the average value and its change were calculated. The measurement units of change based on intercept, slope (speed of change), amplitude, and LST phase were K, K/year, K, and days, respectively.

## 3. Results

### *3.1. Selection of Landsat Data Using QA Tools*

The percentages of images and clearly observed pixels as a cumulative histogram of the study area from the 552 downloaded scenes are presented in Figure 6. Based on this information, if images with a percentage of contaminated pixels ≤10% were selected, approximately 16% of the total scenes could be utilized. These images contained approximately 50% clearly observed pixels; therefore, approximately 50% of the clearly observed pixels were ignored.

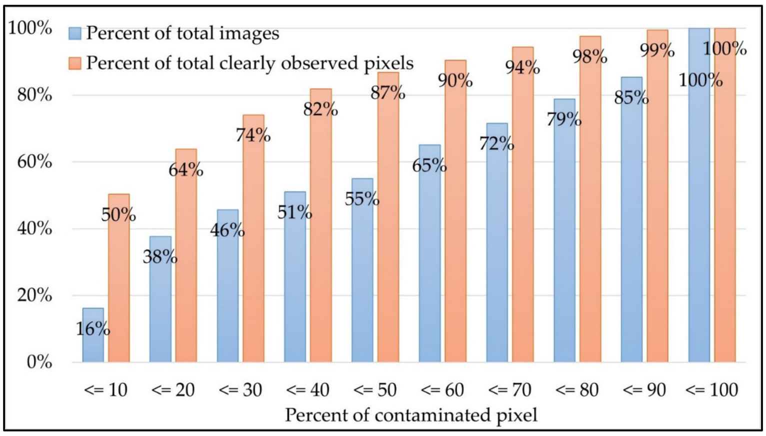


**Figure 6.** Comparison between the percentage of total images and percentage of total clearly observed pixels.

In this study, the images with a percentage of contaminated pixels ≤50% were chosen. Through this selection, the percentage of total images was reduced from 100% (552 scenes) to 55% (305 scenes), but this 55% of images contained 87% of the total clearly observed pixels, i.e., when 45% of the images were removed, only 13% of clearly observed pixels were ignored. Finally, 78 images from Landsat 5, 165 images from Landsat 7, and 62 images from Landsat 8, with a total of 305 images, were selected for further data analysis in this study.

After recognizing the pixel quality with Landsat QA tools, the clearly observed digital values and contaminated pixels of all the chosen images were 1 and 0, respectively. Figure 7 shows the example of the distribution of clearly observed and contaminated pixels from Landsat 5 and 7. The contaminated pixels in Figure 7a primarily resulted from cloud and cloud shadow, while the contaminated pixels in Figure 7b comprise cloud, cloud shadow, and gaps.

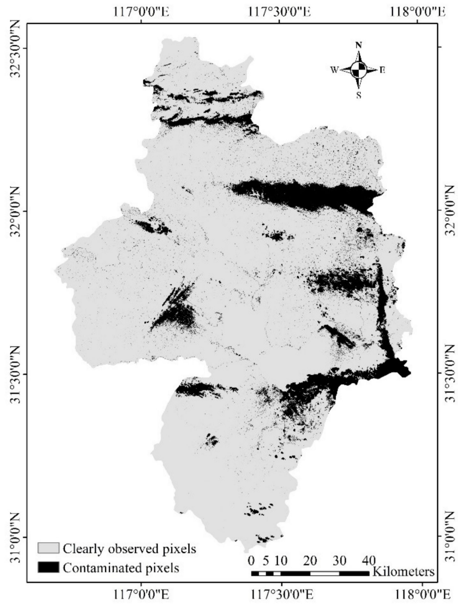


(a)

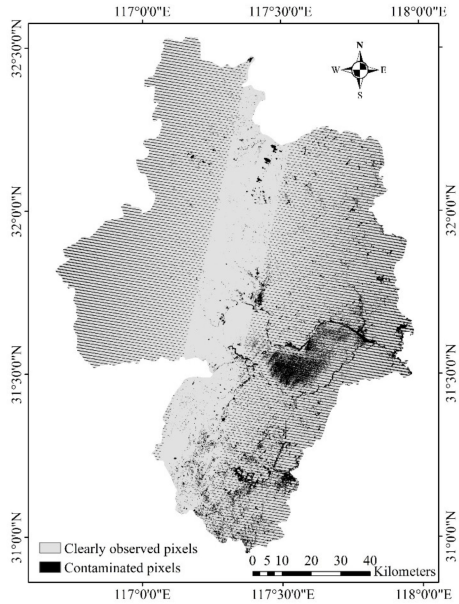


(b)

**Figure 7.** Two examples of clearly observed and contaminated pixels in Hefei City: (**a**) Landsat 5, date 11 May 2003, and (**b**) Landsat 7, date 17 May 2011.

### *3.2. Multitemporal LULC Classification and Change Detection*

The results of the chosen multitemporal LULC maps in 2001, 2006, 2014, and 2020 from time-series Landsat datasets between 2001 and 2020 are displayed in Figure 8.

Table 3 shows the area and percentage of the annual LULC after mode filtering (major filtering) of 13 LULC maps in 2001, 16 LULC maps in 2006, 14 LULC maps in 2014, and 11 LULC maps in 2020.

**Table 3.** Areas and percentages of classified LULC map in 2001, 2006, 2014, and 2020.

| LULC Type | 2001 | | 2006 | | 2014 | | 2020 | |
|---|---|---|---|---|---|---|---|---|
| | Area (km$^2$) | % | Area (km$^2$) | % | Area (km$^2$) | % | Area (km$^2$) | % |
| Urban and built-up land | 234.75 | 2.05 | 433.91 | 3.78 | 1051.66 | 9.17 | 1519.30 | 13.25 |
| Agricultural land | 9342.94 | 81.49 | 9039.13 | 78.84 | 8399.09 | 73.25 | 7422.05 | 64.73 |
| Forest land | 920.98 | 8.03 | 915.82 | 7.99 | 975.61 | 8.51 | 1458.83 | 12.72 |
| Water bodies | 966.98 | 8.43 | 1076.78 | 9.39 | 1039.29 | 9.06 | 1065.47 | 9.29 |
| Total | 11,465.65 | 100 | 11,465.65 | 100 | 11,465.65 | 100 | 11,465.65 | 100 |

The percentage of urban and built-up land increased from 2.05% in 2001 to 13.25% in 2020. Meanwhile, the percentage of forest land and water bodies increased from 8.03% and 8.43% in 2001 to 12.72% and 9.29% in 2020, respectively. In contrast, the proportion of agricultural land declined from 81.49% in 2001 to 64.73% in 2020.

The results show that urban and built-up land in Hefei City underwent a dramatic increase due to urbanization from 2001 to 2020. The expansion of urban and built-up land is presented in Figure 9.

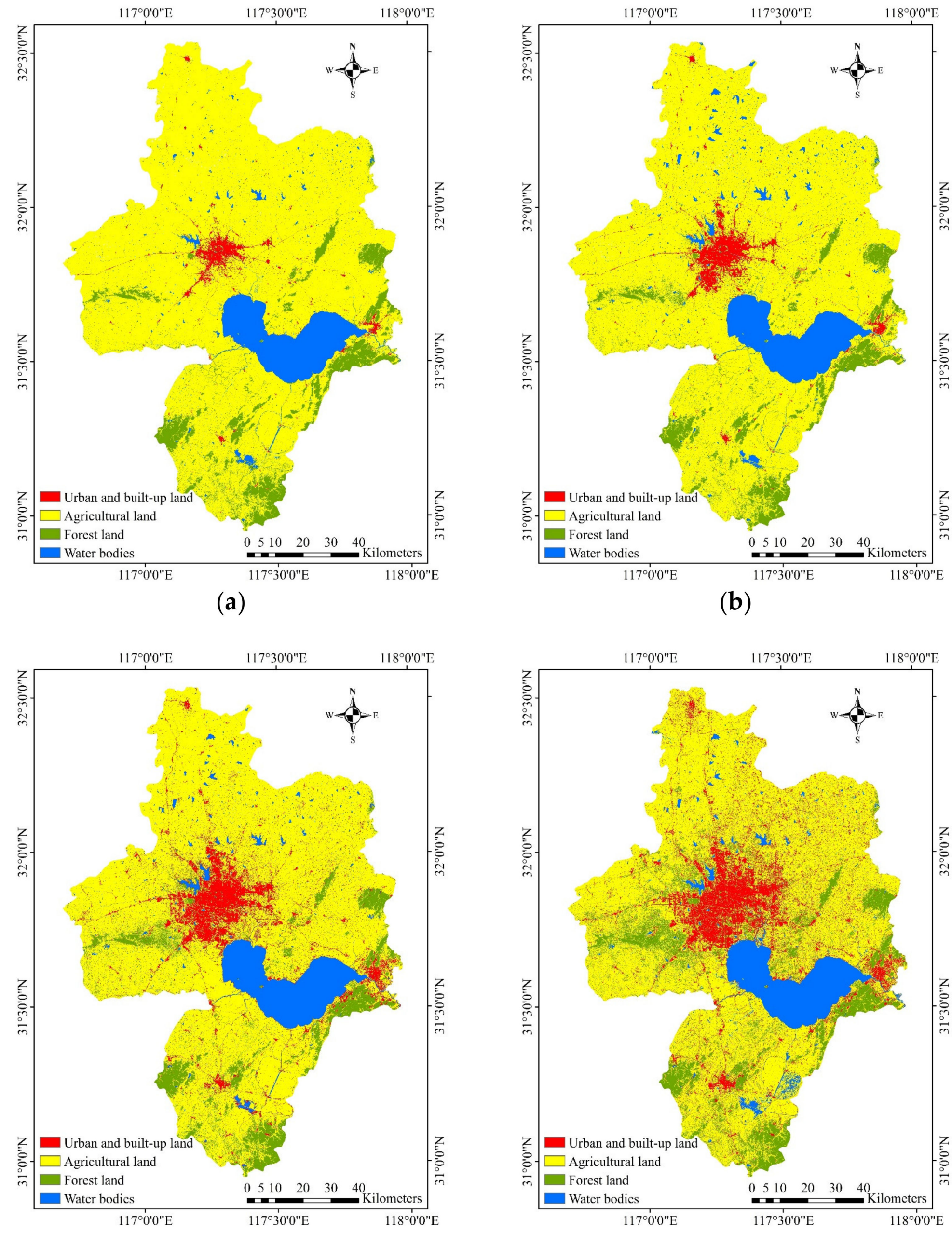


**Figure 8.** Spatial distribution of classified LULC map in: (**a**) 24 July 2001; (**b**) 28 June 2006; (**c**) 5 August 2014; and (**d**) 5 August 2020.

This result highlight that urban and built-up land from 2001 to 2006 expanded outward from the downtown area of Hefei City, and newly developed areas emerged around this core area, covering an area of 199.16 km$^2$. Furthermore, newly emerging developed urban and built-up land from 2006 to 2014 still occurred within the extent of the downtown area of Hefei City, while most newly emerging developed land was expanded in the southwest and south (Chaohu direction) of the city, covering an area of 617.75 km$^2$. In addition, Hefei City continued to expand outward during 2014 and 2020, and the urban and built-up land of the four urban districts (Shushan, Luyang, Yaohai, and Baohe) and the two neighboring counties (Feidong and Feixi) was connected. In contrast, the urban and built-up lands of two outlying counties (Changfeng and Lujiang) and one county-level city (Chaohu) far from the downtown area of Hefei City have been independently expanding outward in the past 20 years.

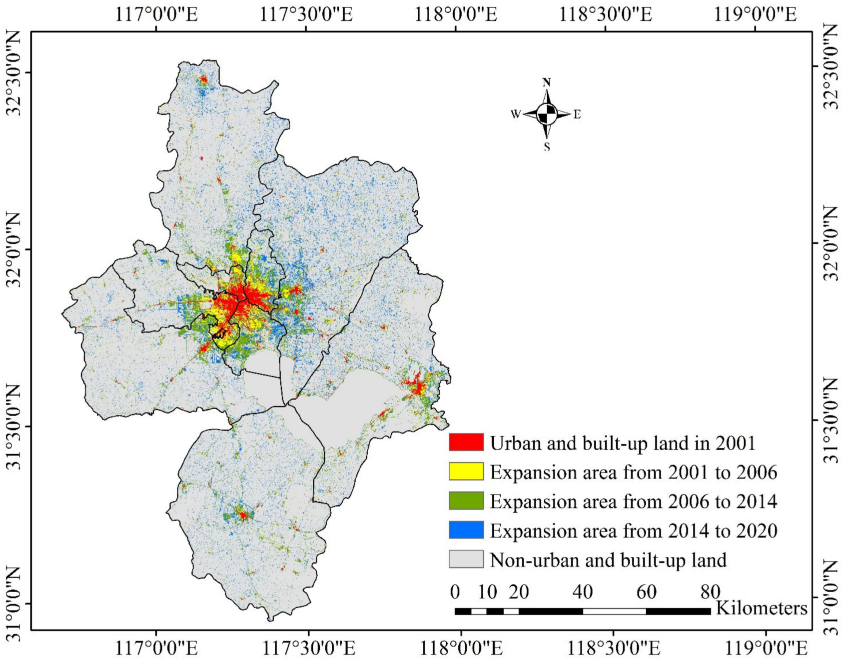


**Figure 9.** The urban and built-up land in 2001 and its expansion.

### 3.3. Thematic Accuracy Assessment

The thematic accuracy assessment was performed using 443 samples, which were selected based on the multinomial distribution, with the desired precision of 5% and a confidence level of 85%. Table 4 presents the error matrix and thematic accuracy on 24 July 2001, 28 June 2006, 5 August 2014, and 5 August 2020.

**Table 4.** Error matrix and thematic accuracy of LULC classification in 2001, 2006, 2014, and 2020.

| Year | | LULC | Reference Information Test Class | | | | Row Total | PA (%) | UA (%) | OA (%) | Kappa Hat (%) |
|---|---|---|---|---|---|---|---|---|---|---|---|
| | | | U | A | F | W | | | | | |
| 2001 | Map class | U | 42 | 6 | 2 | 0 | 50 | 93.33 | 84.00 | 93.00 | 87.97 |
| | | A | 3 | 254 | 2 | 1 | 260 | 92.03 | 97.69 | | |
| | | F | 0 | 11 | 55 | 0 | 66 | 91.67 | 83.33 | | |
| | | W | 0 | 5 | 1 | 61 | 67 | 98.39 | 91.04 | | |
| | Column Total | | 45 | 276 | 60 | 62 | 443 | | | | |
| 2006 | Map class | U | 45 | 5 | 0 | 0 | 50 | 88.24 | 90.00 | 91.65 | 85.56 |
| | | A | 6 | 252 | 4 | 3 | 265 | 91.97 | 95.09 | | |
| | | F | 0 | 10 | 51 | 1 | 62 | 91.07 | 82.26 | | |
| | | W | 0 | 7 | 1 | 58 | 66 | 93.55 | 87.88 | | |
| | Column Total | | 51 | 274 | 56 | 62 | 443 | | | | |
| 2014 | Map class | U | 45 | 6 | 1 | 0 | 52 | 83.33 | 86.54 | 91.42 | 83.79 |
| | | A | 8 | 273 | 3 | 5 | 289 | 93.17 | 94.46 | | |
| | | F | 1 | 7 | 42 | 0 | 50 | 91.30 | 84.00 | | |
| | | W | 0 | 7 | 0 | 45 | 52 | 90.00 | 86.54 | | |
| | Column Total | | 54 | 293 | 46 | 50 | 443 | | | | |
| 2020 | Map class | U | 52 | 12 | 0 | 1 | 65 | 94.55 | 80.00 | 90.52 | 83.13 |
| | | A | 3 | 257 | 3 | 2 | 265 | 88.62 | 96.98 | | |
| | | F | 0 | 17 | 46 | 0 | 63 | 93.88 | 73.02 | | |
| | | W | 0 | 4 | 0 | 46 | 50 | 93.88 | 92.00 | | |
| | Column Total | | 55 | 290 | 49 | 49 | 443 | | | | |

As a result, the OA from the four maps varied from 90.52% to 93.00%, with an average value of 91.65%, while the Kappa hat coefficients ranged from 83.13% to 87.97%, with an average value of 85.11%. In addition, the average PA of each LULC type from the four maps, which is a measure of omission error [62], varied from 83.33% for urban and built-up land to 98.39% for water bodies. Meanwhile, the average UA of each LULC type, which is a measure of the commission error [62], varied from 73.02% for forest land to 97.69% for agricultural land.

### 3.4. Estimation of Time-Series LST Dataset

All selected 305 images were adopted to estimate LST using the SC method. Figure 10 presents an example of the three primary pre-processing products, including BT, emissivity, and atmospheric water vapor content, and the LST result. It can be clearly observed that the BT in the central urban area was higher than the BT of Chaohu Lake in the southeast. In addition, the emissivity of water bodies was higher, while urban and built-up land emissivity was lower. Furthermore, the atmospheric water vapor content in the north of Chaohu Lake was higher, while most land areas' atmospheric water vapor content was lower. Furthermore, LST distribution was roughly the same as BT, but lower and upper boundary values of LST were higher than BT.

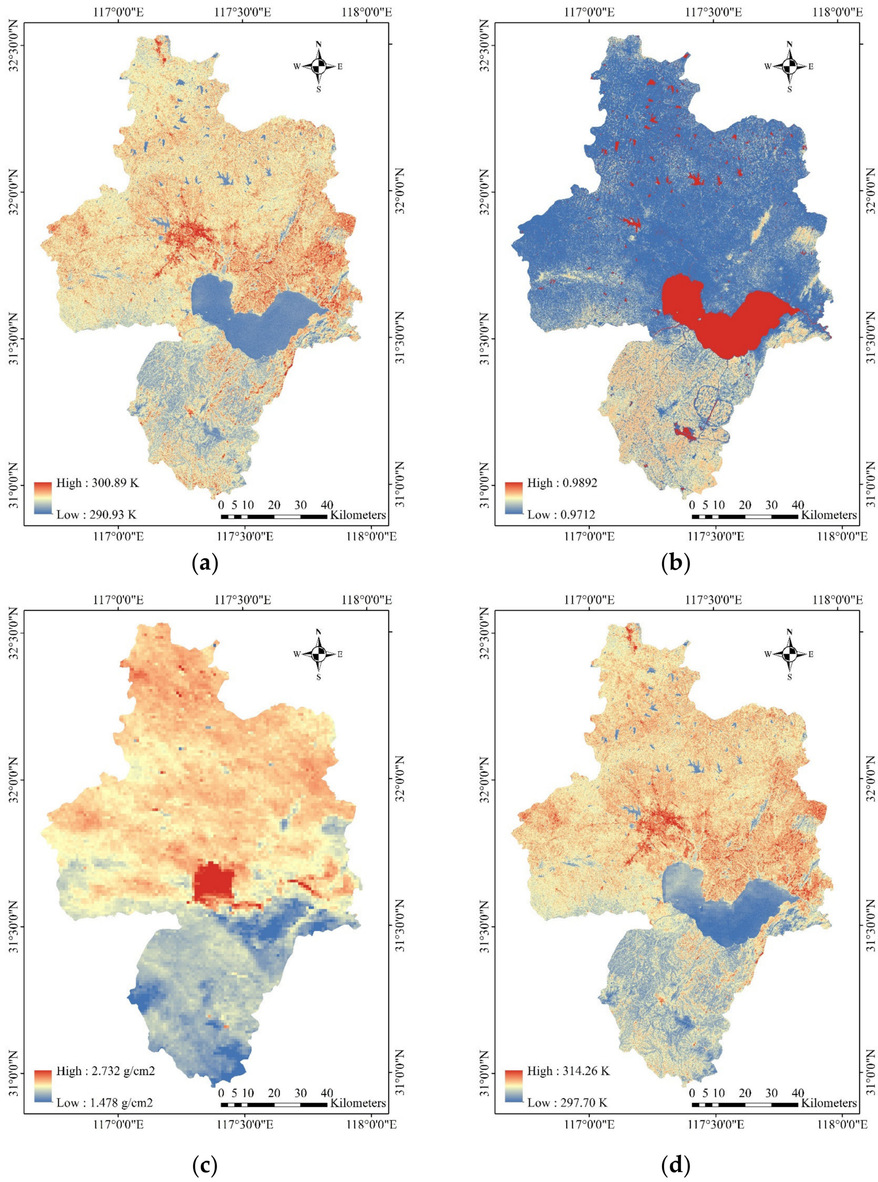


**Figure 10.** Spatial distribution LST with the three primary pre-processing products from Landsat TM, date 29 September 2002: (**a**) BT, (**b**) emissivity, (**c**) water vapor content, and (**d**) LST.

### 3.5. Reconstruction of Time-Series LST Dataset

The LST values estimated from the contaminated pixels in the images are usually inaccurate. Therefore, it is necessary to reconstruct the LST values of these pixels. Figure 11 shows an example of one pixel (Point_AU in Figure 1) from 305 selected scenes according to the processing steps of LST reconstruction.

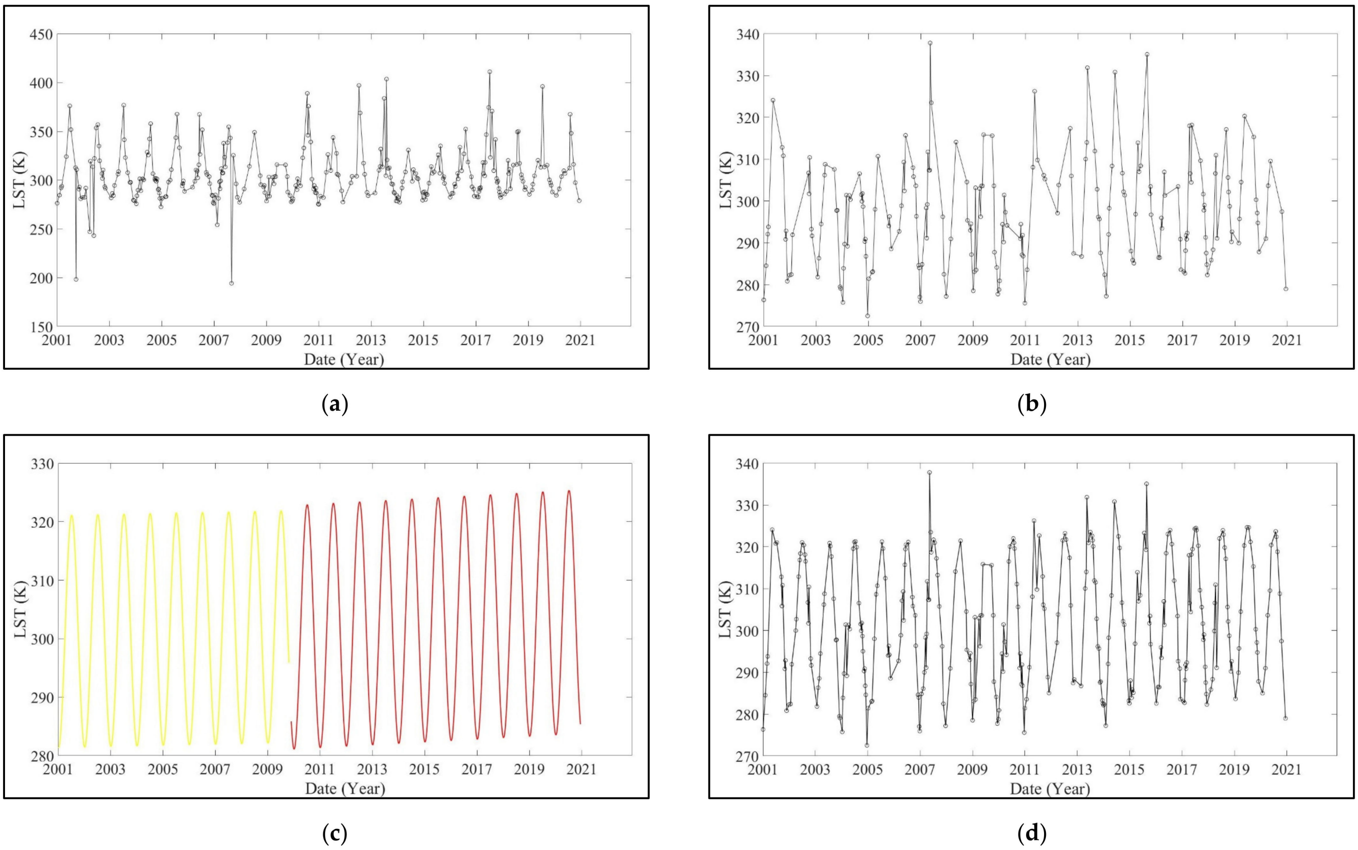


(**a**) (**b**) (**c**) (**d**)

**Figure 11.** Primary calculation process and results of one pixel. (**a**) Estimated LST values (305 scenes); (**b**) estimated LST data after ignoring contaminated values (185 scenes); (**c**) simulated LST recalculated using HA for each period based on harmonic terms (305 scenes); and (**d**) reconstructed time-series LST (305 scenes).

Figure 11a shows the estimated LST data of one pixel from 305 scenes. It reveals that most of the LST values oscillated above and below 300 K, but some of the values from some scenes were very high or very low (e.g., around the years 2002 and 2008). Figure 11b shows the estimated LST data of one pixel after ignoring contaminated values. As a result, only 185 scenes remain, and the extreme values have been removed. Most of the LST values varied between 270 and 330 K. It is also clear that the LST value fluctuated 20 times with the seasons (corresponding to the Landsat data from 2001 to 2020). Figure 11c shows simulated LST data using HA for each segmented LULC period based on harmonic terms. As a result, the remaining 185 scenes of this pixel were divided into two periods according to the LULC type. Among them, the yellow curve represents the simulated LST of agricultural land (first period), and the red curve represents the simulated LST of urban and built-up land (second period). Then, the harmonic function parameters could be simulated for each period. Meanwhile, the simulated LST data of 305 scenes were recalculated from the parameters. Figure 11d shows the reconstructed time-series LST of 305 scenes of this pixel.

Meanwhile, Figure 12 shows the examples of the estimated, simulated, reconstructed LST data and the differences between the estimated LST and reconstructed LST for 11 May 2003. In Figure 12a, it can be seen that the LST data in the northeast of the city were significantly underestimated (blue color), and this area is approximately consistent with the contaminated area in the northeast in Figure 7a. In addition, Figure 12b shows the simulated LST data, whose values in this scene were calculated from harmonic terms. Figure 12c shows the reconstructed LST, where the underestimated LST in the northeast and other areas of the city has been corrected using the simulated LST. Figure 12d shows the difference between the estimated LST and reconstructed LST (estimated LST–reconstructed LST), and the estimated LST of the contaminated pixel is more than 3 K lower than the reconstructed LST (blue color).

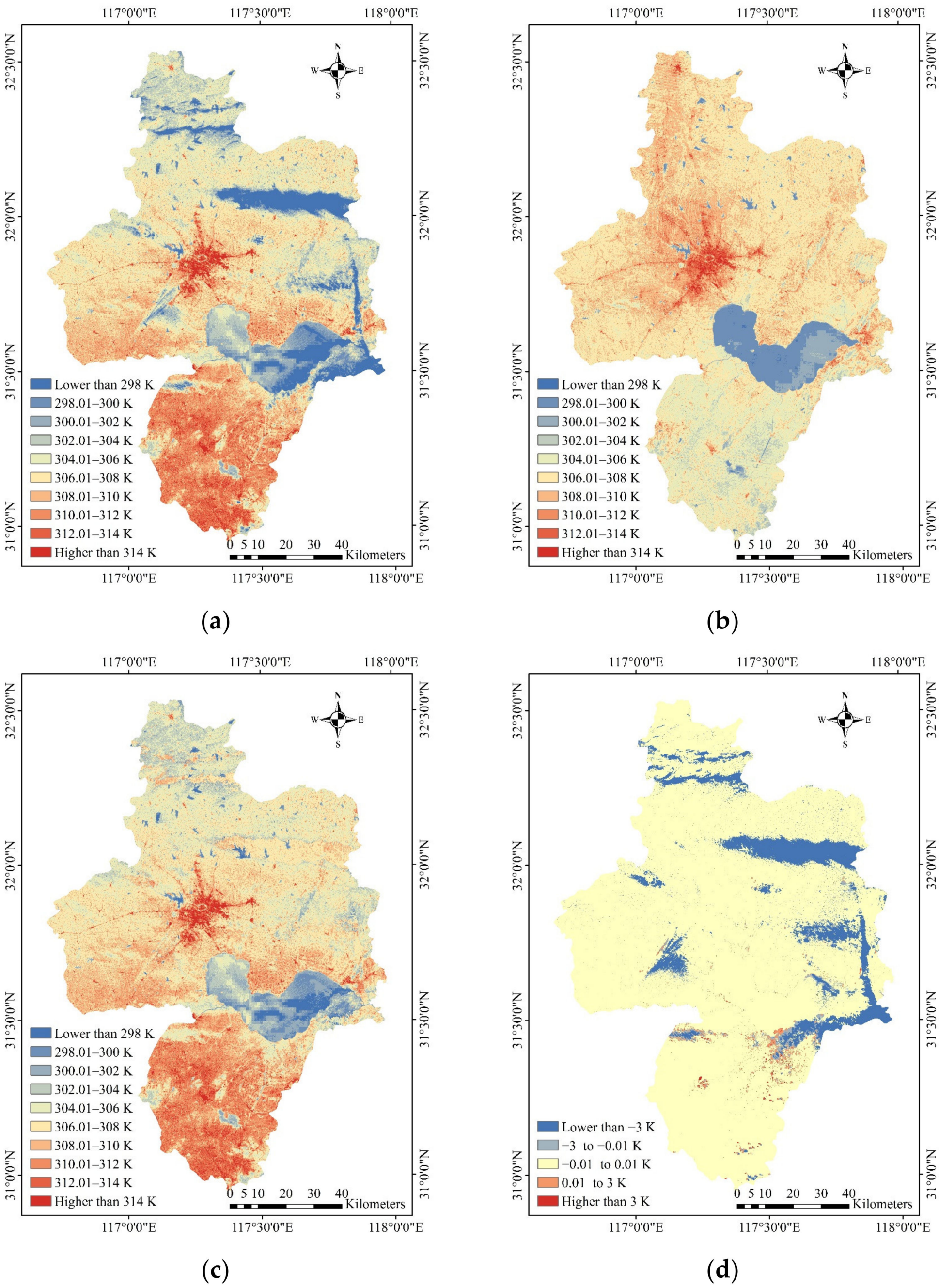


**Figure 12.** Reconstruction of LST product from different processing steps, date: 11 May 2003: (**a**) estimated LST; (**b**) simulated LST; (**c**) reconstructed LST; and (**d**) estimated LST—reconstructed LST.

The *ME* value between the simulated LST using the HA model and the estimated LST using the SC method on clearly observed pixels was 0.03 K. Simultaneously, the *MAE*, which ignores positive and negative offset, was 1.54 K. As a result, the replacement of estimated LST with simulated LST on the contaminated pixels can be accepted because the *ME* value is less than 1 K. The multitemporal LST maps on 21 May 2001, 27 May 2006, 1 May 2014, and 17 May 2020, which were selected from the time-series LST dataset between 2001 and 2020, are presented in Figure 13. It is easy to see that the spatial distribution of the LST in Figure 13 was highly related to the LULC type in Figure 8. The urban and built-up land had the highest LST value, followed by agricultural land and forest land. On the contrary, the LST value in water bodies was the lowest.

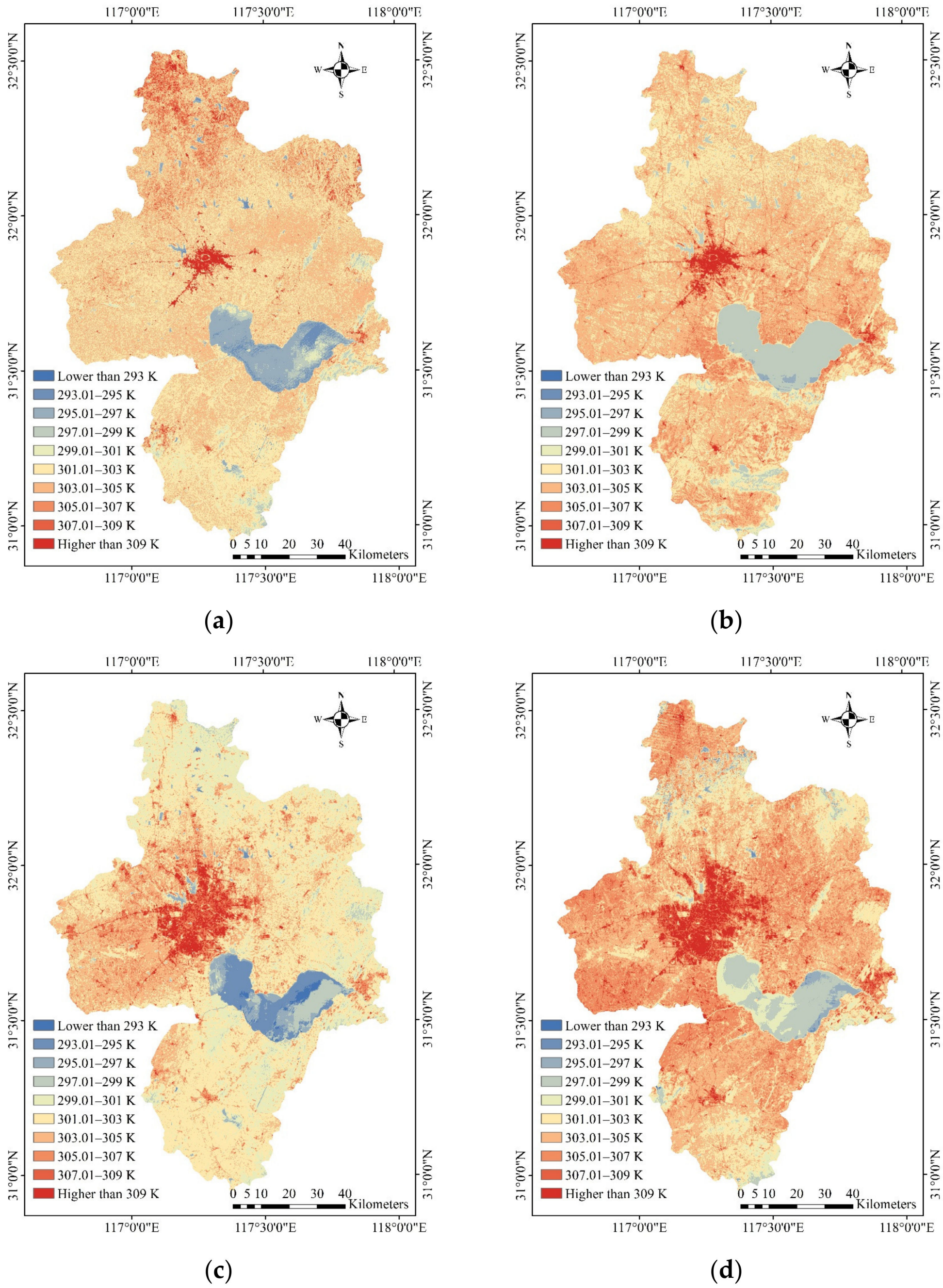


**Figure 13.** Spatial distribution of LST: (**a**) 21 May 2001; (**b**) 27 May 2006; (**c**) 1 May 2014; and (**d**) 17 May 2020.

### *3.6. Impact of LULC Change on LST*

#### 3.6.1. Impact of LULC Change on LST Using Spatial Analysis (Space Domain)

Table 5 shows the area and mean LST of urban and non-urban land use types in 2001, 2006, 2014, and 2020 at five different research areas (the whole Hefei City, four urban districts (Shushan, Luyang, Yaohai, and Baohe), two counties closed to urban districts (Feidong, and Feixi), two counties faraway from urban districts (Changfeng, and Lujiang), and one county-level city (Chaohu)). Regardless of the scale and year, the LST in urban areas is higher than that in non-urban areas, but these differences are not the same for different scales and different years. Meanwhile, the LST of urban areas in different districts/counties/subordinate-city is also different compared with the LST of urban areas in the whole Hefei City. As the scope of urban area in Shushan, Luyang, Yaohai, and Baohe increased from 138.49 km$^2$ in 2001 to 474.66 km$^2$ in 2020, the LST also increased from 298.11 K to 304.94 K. In addition, the finding of the urban area of four urban districts is in line with the report of the Statistics Bureau of Anhui Province [44], reporting that built-up areas in four urban districts of Hefei City increased from 125.00 km$^2$ in 2001 to 481.00 km$^2$ in 2019.

**Table 5.** Area and mean LST of urban and non-urban types in 2001, 2006, 2014, and 2020.

| Research Area | LULC Type * | 2001 | | 2006 | | 2014 | | 2020 | |
|---|---|---|---|---|---|---|---|---|---|
| | | Area (km$^2$) | Mean LST ** (K) | Area (km$^2$) | Mean LST (K) | Area (km$^2$) | Mean LST (K) | Area (km$^2$) | Mean LST (K) |
| Hefei City | Urban | 234.75 | 298.11 | 433.91 | 302.06 | 1051.66 | 298.17 | 1519.30 | 303.09 |
| | Non-Urban | 11230.90 | 295.81 | 11031.73 | 297.99 | 10413.99 | 295.29 | 9946.34 | 299.52 |
| Shushan, Luyang, Yaohai, and Baohe | Urban | 138.49 | 298.11 | 258.71 | 302.57 | 419.74 | 299.18 | 474.66 | 304.94 |
| | Non-Urban | 1182.01 | 295.05 | 1061.78 | 298.27 | 900.75 | 295.79 | 845.84 | 300.36 |
| Feidong and Feixi | Urban | 40.03 | 297.92 | 72.45 | 301.31 | 263.54 | 297.99 | 486.34 | 302.73 |
| | Non-Urban | 3849.83 | 296.01 | 3817.42 | 298.25 | 3626.32 | 295.98 | 3403.53 | 300.47 |
| Changfeng and Lujiang | Urban | 23.38 | 298.12 | 60.38 | 301.49 | 223.06 | 297.51 | 364.55 | 301.64 |
| | Non-Urban | 4164.86 | 295.98 | 4127.86 | 298.13 | 3965.19 | 295.33 | 3823.69 | 299.17 |
| Chaohu City | Urban | 32.81 | 298.29 | 42.34 | 301.00 | 145.32 | 296.47 | 193.71 | 302.14 |
| | Non-Urban | 2034.23 | 295.50 | 2024.70 | 297.03 | 1921.72 | 293.70 | 1873.34 | 298.14 |

* Urban: urban and built-up land; non-urban: agricultural land, forest land, and water bodies. ** The LST in 2001, 2006, 2014, and 2020 in this table refers to the median composite of 13 LST maps in 2001, 16 LST maps in 2006, 14 LST maps in 2014, and 11 LST maps in 2020, respectively.

Meanwhile, the LST of urban area in Feidong and Feixi increased from 297.92 K to 302.73 K when the range increased from 40.03 km$^2$ to 486.34 km$^2$. In the meantime, the LST of urban areas in Changfeng and Lujiang increased from 298.12 K to 301.64 K when the area increased from 23.38 km$^2$ to 364.55 km$^2$. Moreover, the scope of urban area in Chaohu City increased from 32.81 km$^2$ in 2001 to 193.71 km$^2$ in 2020; the LST also increased from 298.29 K to 302.14 K.

Figure 14a shows the differences of LST between urban and non-urban areas. For the whole Hefei City scale, the difference of LST between urban and non-urban areas is gradually increasing, which rose from 1.52 K in 2001 to 3.57 K in 2020. The LST difference between urban and non-urban areas in Shushan, Luyang, Yaohai, and Baohe districts is even greater, increasing from 3.06 K in 2001 to 4.58 K in 2020. However, the difference of LST between urban and non-urban areas in Changfeng and Lujiang counties is small, growing from 2.14 K in 2001 to 2.47 K in 2020. Therefore, the difference of LST between urban and non-urban areas in 2020 is higher than in 2001.

Figure 14b shows the difference of LST of the urban areas between four small research areas and the Hefei City. For Shushan, Luyang, Yaohai, and Baohe districts, which are the center of Hefei City, the LST is high than the average LST of whole Hefei City, the differences of LST are 0.41 K, 1.04 K, 1.01 K, and 1.78 K in 2001, 2006, 2014, and 2020, respectively. For Feidong and Feixi counties, close to the center of Hefei City, as the urban area was relatively isolated and surrounded by lots of non-urban areas before 2006, the LST is lower (−0.60 K in 2001 and −1.38 K in 2006) than the average LST of whole Hefei City. With the urban growth, a filling and axial expansion appeared, and the urban areas of these two counties were almost integrated with the Shushan, Luyang, Yaohai, and Baohe districts. The LST is almost the same (−0.14 K in 2014 and 0.04 K in 2020) as the average LST of whole Hefei City. For Changfeng and Lujiang counties, which are far away from the center of Hefei City, the urban area was developing in isolation for a long time; therefore, the LST of urban area is lower than the Hefei City's average. Due to the uneven regional development, this difference is getting bigger (−0.65 K in 2001, −1.86 K in 2020). For Chaohu City, a county-level city (subordinate cities of Hefei City), located in the east of Chaohu Lake, the LST of the urban area was close to the average LST of the whole Hefei City in 2001 (−0.23 K). Since then, the LST in the urban area has been lower than the average LST in the urban area of the whole Hefei City.

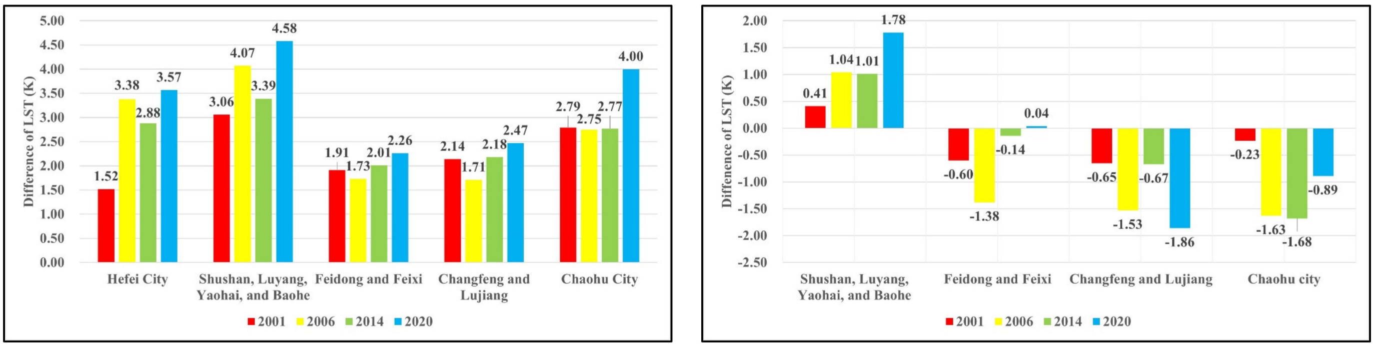


(**a**) (**b**)

**Figure 14.** The difference of LST in 2001, 2006, 2014, and 2020 between: (**a**) urban and non-urban area; (**b**) four small research areas and the Hefei city in urban area.

This finding is an expected result because when another land cover is transformed into urban and built-up land, LST will be increased. These phenomena indicate the impact of LULC change on LST when the other land cover types, i.e., agricultural land, forest land, and water bodies, are converted to urban and built-up land. Another finding is that the difference of LST between urban and non-urban areas is becoming larger, and LST has an obvious spatial agglomeration effect. The LST of small fragmented urban areas is easily affected by the surrounding non-urban areas, which can help cool the LST, leading to smaller differences in LST between urban and non-urban areas. With the development of the city, the fragmented urban land gradually expands and merges to form large contiguous areas. The surrounding non-urban areas have no obvious cooling effect on them, resulting in a greater LST difference between urban and non-urban areas. In addition, the LST of these contiguous urban areas is also higher than that of the fragmented urban areas.

#### 3.6.2. Impact of LULC Change on LST using Decomposition Analysis (Time Domain)

The impact of LULC change on LST using decomposition analysis is separately described and discussed in this section.

(1) Calculation and verification of harmonic terms of LST

Figure 15 shows the results of the decomposition analysis using time-series LST at four points (Point_U from urban and built-up land, Point_A from agricultural land, Poin_F from forest land, and Point_W from water bodies, See Figure 1) from LULC unchanged areas. In detail, Figure 15a,c,e,g demonstrate the estimated LST (black circles) and simulated LST (trend component + seasonality component, blue curve) for urban and built-up land, agricultural land, forest land, and water bodies, respectively. Figure 15b,d,f,h show LST residuals (the difference between estimated LST and simulated LST) of urban and built-up land, agricultural land, forest land, and water bodies, respectively.

As a result, the mean residuals for selected four points from four different LULC types are 0.22 K, 0.12 K, −0.49 K, and 0.02 K, respectively, which are close to zero. Meanwhile, the residuals fluctuate around zero without exhibiting evident patterns. In other words, the residual distribution is close to a normal distribution with a mean of zero. These low and randomly distributed residuals mean that the error is small when estimated LST is represented by the sum of the trend and seasonality components. Thus, it is possible to analyze the effect of LULC change on LST using the trend component and seasonality component of LST in the time domain with a small error.

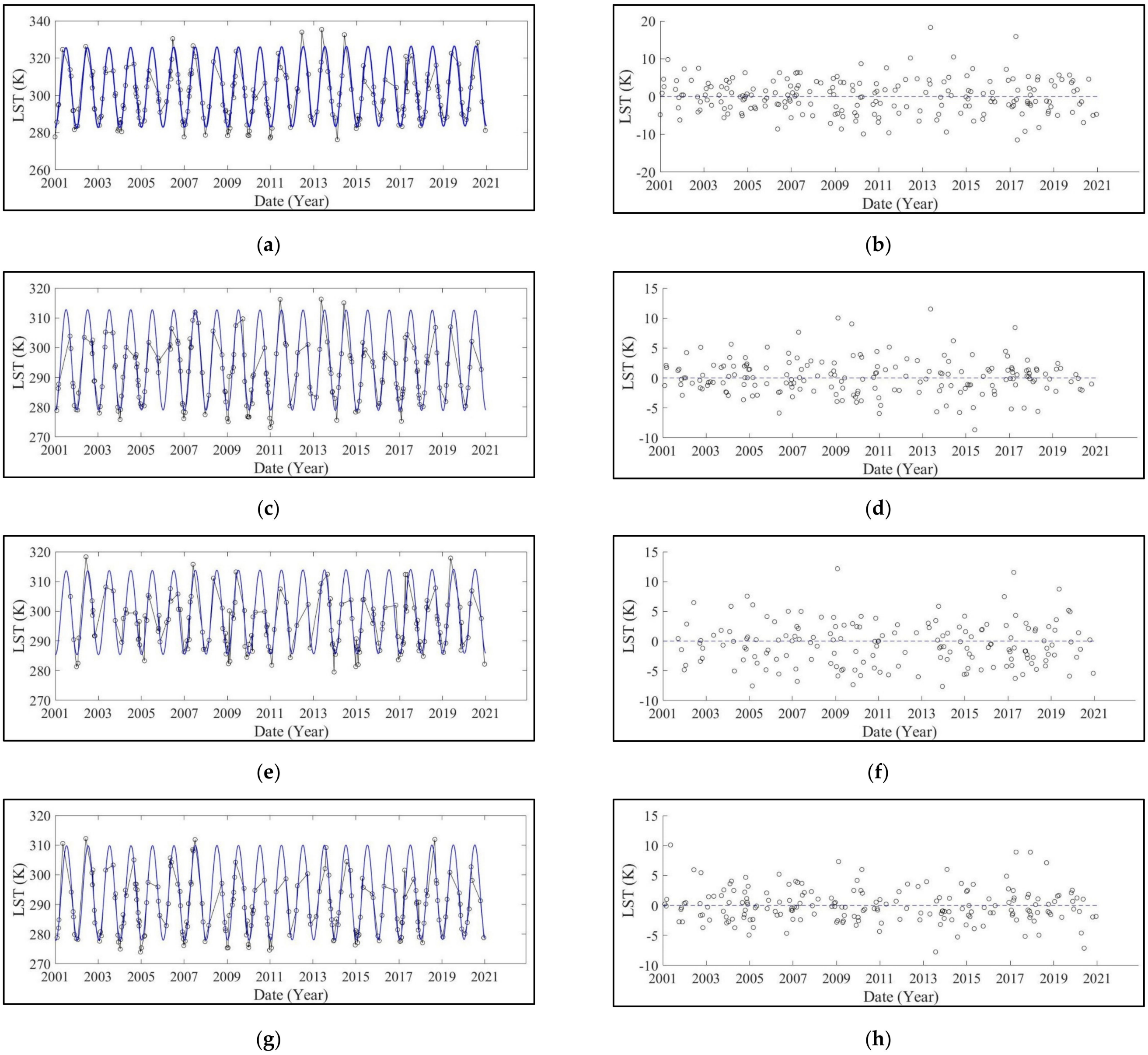


**Figure 15.** Examples of estimated LST data (after ignoring contaminated value), modeled LST and residuals: (**a**) estimated and simulated LST at Point_U where LULC type is urban and built-up land, (**b**) residuals at Point_U, (**c**) estimated and simulated LST at Point_A where LULC type is agricultural land, (**d**) residuals at Point_A, (**e**) estimated and simulated LST at Point_F where LULC type is forest land, (**f**) residuals at Point_F, (**g**) estimated and simulated LST at Point_W where LULC type is water bodies, (**h**) residuals at Point_W.

Table 6 shows the regression equations for the LST simulation that have been used in Figure 16. The root mean square errors (RMSE) of LST simulation for urban and built-up land, agricultural land, forest land, and water bodies are 4.465, 3.576, 3.681, and 2.808, respectively. Meanwhile the coefficients of determination ($R^2$) are 0.8819, 0.9019, 0.8012, and 0.9038. The low RMSE and high $R^2$ testify to good modeling for LST. Due to the stability of the water body, its RMSE is smaller than other LULC types, and $R^2$ is greater than other types. The amplitude value of LST in urban areas (21.54 K) is higher than that in non-urban areas (16.89 K, 14.16 K and 15.96 K), indicating the LST difference between summer and winter in urban areas is larger, while the LST difference in non-urban areas is smaller. Furthermore, the intercept value of LST in urban areas (304.1 K) is also higher than that in non-urban areas (295.5 K, 299.5 K and 293.8 K), which implies that the LST of the urban area is higher than the non-urban area in the year of 2001 (starting date of the model).

**Table 6.** LST regression equation for LST modeling using linear trend component and seasonality component.

| LULC Type | Regression Equation | RMSE | $R^2$ |
|---|---|---|---|
| Urban and built-up land | $LST = 304.1 + 1.34 \times 10^{-4} \times t + 21.54 \times \cos(2 \times pi \times t/365 - 3.19)$ | 4.465 | 0.8819 |
| Agricultural land | $LST = 295.5 - 0.31 \times 10^{-4} \times t - 16.89 \times \cos(2 \times pi \times t/365 - 9.57)$ | 3.576 | 0.9019 |
| Forest land | $LST = 299.5 + 0.70 \times 10^{-4} \times t - 14.16 \times \cos(2 \times pi \times t/365 - 3.20)$ | 3.681 | 0.8012 |
| Water bodies | $LST = 293.8 + 0.44 \times 10^{-4} \times t + 15.96 \times \cos(2 \times pi \times t/365 + 15.52)$ | 2.808 | 0.9038 |

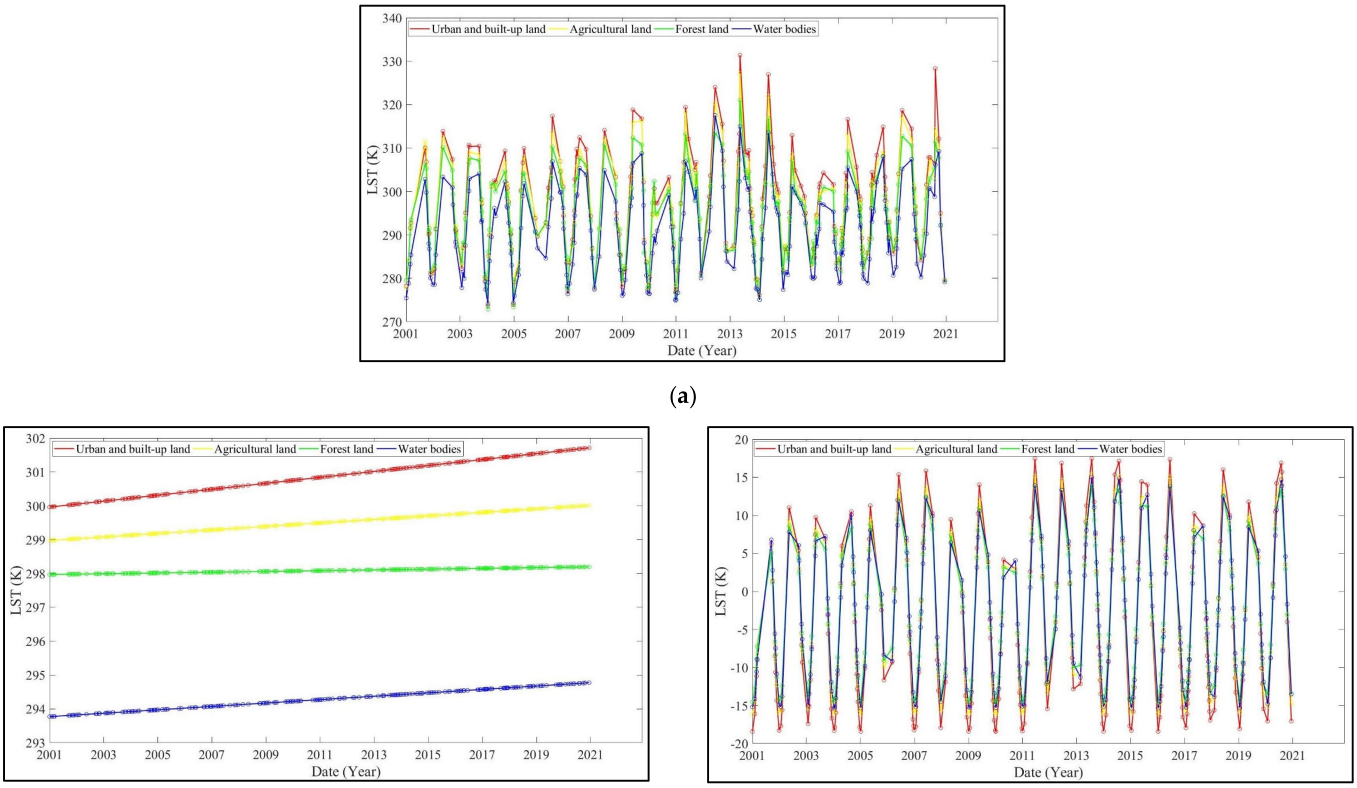


(**a**)

(**b**) (**c**)

**Figure 16.** Mean LSTs of four different LULC types and their trend and seasonality components: (**a**) mean LSTs; (**b**) trend component of LST; and (**c**) seasonality component of LST.

Table 7 shows the regressions equation for LST simulation using the sum of non-linear trend component and seasonality component for different LULC types. In Table 7, the intercept values (304.7 K, 295.9 K, 299.8 K, and 294.0 K) and amplitude values (21.55 K, 16.89 K, 14.14 K, and 15.95 K) are very close to the intercept values and amplitude values in Table 6. This finding suggests that the intercept and amplitude are two key terms for LST regression. Meanwhile, the values of intercept and amplitude in urban are obviously higher than those in a non-urban area. However, the values of RMSE and $R^2$ in Table 7 are also very much the same as those of RMSE and $R^2$ in Table 6, which shows that the regression accuracy is not significantly improved when the complexity of the equation and the amount of calculation are increased.

**Table 7.** LST regression equation for LST modeling using non-linear trend component and seasonality component.

| LULC Type | Regression Equation | RMSE | $R^2$ |
|---|---|---|---|
| Urban and built-up land | $LST = 304.7 - 3.86 \times 10^{-4} \times t + 7.15 \times 10^{-8} \times t^2 + 21.55 \times \cos(2 \times pi \times t/365 - 21.94)$ | 4.467 | 0.8823 |
| Agricultural land | $LST = 295.9 - 1.64 \times 10^{-4} \times t - 0.20 \times 10^{-8} \times t^2 - 16.89 \times \cos(2 \times pi \times t/365 - 3.29)$ | 3.584 | 0.9078 |
| Forest land | $LST = 299.8 - 1.61 \times 10^{-4} \times t + 3.03 \times 10^{-8} \times t^2 - 14.14 \times \cos(2 \times pi \times t/365 - 28.33)$ | 3.691 | 0.8014 |
| Water bodies | $LST = 294.0 - 0.67 \times 10^{-4} \times t + 1.52 \times 10^{-8} \times t^2 + 15.95 \times \cos(2 \times pi \times t/365 - 28.47)$ | 2.815 | 0.9038 |

(2) Harmonic terms of average LST values of different LULC types

Figure 17 shows the mean LST values of different LULC types from every scene (305 scenes) and its trend and seasonality component. Figure 17a shows the average LST values of four different LULC types (U, A, F, and W) with red, yellow, green, and blue curves, respectively. As a result, the average LST values of urban and built-up land on different dates were higher than other LULC types.

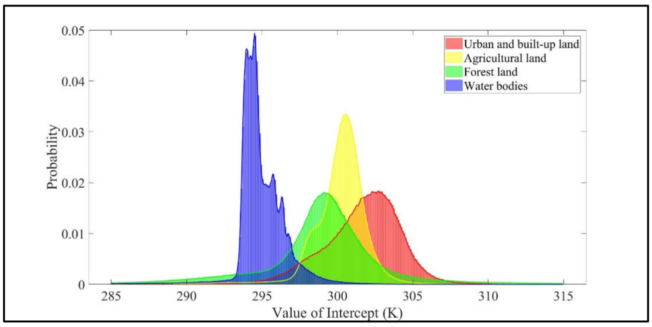


(**a**)

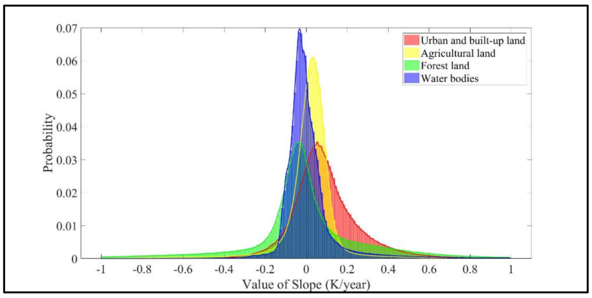


(**b**)

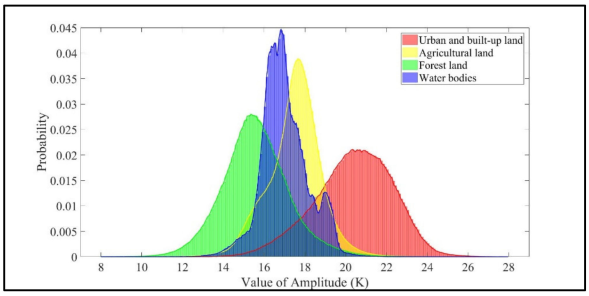


(**c**)

**Figure 17.** Distribution of normalized histogram distribution of harmonic term for four different LULC types: (**a**) intercept term, (**b**) slope term, and (**c**) amplitude term.

In addition, Figure 16b,c illustrate the trend and seasonality component of the mean LSTs of each LULC type after the decomposition procedure. Detailed information of the harmonic terms is provided in Table 8. The intercept term of the trend component suggests that the mean LST values of urban and built-up land, agricultural land, forest land, and water bodies in 2001 were 299.96 K, 298.97 K, 297.96 K, and 293.77 K, respectively. Meanwhile, the slope term of the trend component indicates that the mean LST value increased by 0.09 K/year, 0.05 K/year, 0.01 K/year, and 0.05 K/year for urban and built-up land, agriculture land, forest land, and water bodies, respectively. Additionally, the amplitude term of the seasonality component suggests that the intra-annual variability of urban and built-up land, agricultural land, forest land, and water bodies was 18.43 K, 16.16 K, 14.56 K, and 15.36 K, respectively. In addition, the differences of LST phase values among four LULC types are very small, indicating that the maximum value of LST and the minimum value of LST for different LULC types appear almost on the same time. This finding shows that the average LST, increasing speed of LST, and annual LST change in urban and built-up land were higher than those in other land cover types.

**Table 8.** The trend and seasonality components of mean LSTs of each LULC type.

| LULC Types | Trend Component | | Seasonality Component | |
|---|---|---|---|---|
| | Intercept (K) | Slope (K/Year) | Amplitude (K) | Phase (Days) |
| Urban and built-up land | 299.96 | 0.09 | 18.43 | −0.06 |
| Agricultural land | 298.97 | 0.05 | 16.16 | −0.33 |
| Forest land | 297.96 | 0.01 | 14.56 | 6.21 |
| Water bodies | 293.77 | 0.05 | 15.36 | −3.30 |

(3) Distribution of harmonic terms of LST of different LULC types

The normalized histogram distribution of the three main harmonic terms (intercept, slope, and amplitude) of LST for different LULC segments is displayed in Figure 17. Meanwhile, the mean and variance values of the main harmonic terms of LST of four LULC types are presented in Table 9. As a result, the mean and variance values of the intercept term of LST of four LULC types are 301.64 K, 300.18 K, 298.77 K, 294.90 K, and 2.88 K, 1.92 K, 5.13 K, 3.03 K, respectively. In addition, the mean and variance values of the slope term of LST of four LULC types are 0.105 K/year, 0.016 K/year, 0.003 K/year, 0.013 K/year and 0.194 K/year, 0.154 K/year, 0.367 K/year, 0.149 K/year, respectively. Further, the mean and variance values of the amplitude term of LST of four LULC types are 20.42 K, 17.49 K, 15.61 K, 17.03 K, and 1.90 K, 1.29 K, 1.66 K, 1.14 K, respectively. This finding also indicates that the average LST, increasing speed of LST, and annual LST change in urban areas were higher than those in other land cover types.

**Table 9.** The mean and variance value of the main three harmonic terms.

| LULC Types | Intercept (K) | | Slope (K/year) | | Amplitude (K) | |
|---|---|---|---|---|---|---|
| | Mean | Variance | Mean | Variance | Mean | Variance |
| Urban and built-up land | 301.64 | 2.88 | 0.105 | 0.194 | 20.42 | 1.90 |
| Agricultural land | 300.18 | 1.92 | 0.016 | 0.154 | 17.49 | 1.29 |
| Forest land | 298.77 | 5.13 | 0.003 | 0.367 | 15.61 | 1.66 |
| Water bodies | 294.90 | 3.03 | 0.013 | 0.149 | 17.03 | 1.14 |

(4) Impact of LULC change on harmonic terms of LST

Table 10 lists the mean values of LST harmonic terms from the pixels and demonstrates that their LULC type changed from agricultural land, forest land, and water bodies to urban and built-up land during 2001 and 2020.

**Table 10.** Thermal signatures and thermal signature changes of the LULC change type.

| Change Types | Intercept (K) | | | Amplitude (K) | | |
|---|---|---|---|---|---|---|
| | Before | After | Change | Before | After | Change |
| Agricultural land to urban and built-up land | 300.46 | 302.23 | 1.77 | 19.13 | 20.54 | 1.41 |
| Forest land to urban and built-up land | 300.49 | 301.89 | 1.40 | 17.28 | 19.03 | 1.75 |
| Water bodies to urban and built-up land | 297.05 | 298.50 | 1.45 | 17.75 | 18.62 | 0.87 |

As a result, the difference values of LST in terms of intercept and amplitude are 1.77 K and 1.41 K, in converting agricultural land to urban and built-up land. Meanwhile, in the transformation of forest land to urban and built-up land, the difference values of LST in terms of intercept and amplitude are 1.40 K and 1.75 K. At the same time, in the conversion of water bodies to urban and built-up land, the difference values of LST in terms of intercept and amplitude are 1.45 K and 0.87 K.

In summary, when other types of LULC are converted to urban and built-up land, their intercept and amplitude values will increase. This finding is similar to the values of the harmonic parameters shown in Figure 17; in other words, the intercept and amplitude values of urban and built-up land are higher than those of other LULC types. This finding implies that the average LST and annual LST change in urban areas are higher than those in other non-urban areas.

## 4. Discussion

### *4.1. Landsat Image Selection*

The number of finally selected Landsat scenes between 2001 and 2020 in this study was reduced by 45% (from 552 to 305 scenes) through contaminated pixel recognition and assessment based on the Landsat QA band. The strength of this procedure lies in two aspects: a decrease in the number of Landsat scenes and the cost of data analysis, and recognition of the clearly observed and contaminated pixels. However, the percentage and distribution of clearly observed and contaminated pixels must be identified, calculated, and evaluated according to information from the Landsat QA band.

### *4.2. Multitemporal LULC Classification and Change Detection and Accuracy Assessment*

Multitemporal LULC classification and change detection were successfully conducted using the algorithm proposed by Sun and Ongsomwang [42] in this research. This approach can be used to quickly classify and map LULC data and their changes at any time and period. According to the thematic accuracy assessment, as reported in Section 3.3, the OA value of LULC maps in 2001, 2006, 2014, and 2020 and its average are higher than 90%. This finding indicates that the classified maps can provide acceptable results, as recommended by [63]. Likewise, the Kappa hat values of the four maps are higher than 80%; they represent strong agreement or accuracy between the classified LULC map and the ground reference data [64].

Moreover, the derived overall accuracy is comparable with other studies. For instance, Marco et al. [65] applied 281,962 Landsat scenes to classify a series of land cover maps at continental scale for Australia between 1993 and 2008 at a 5-year time-step using Google Earth Engine (GEE), with an OA of approximately 93%. Zhu and Woodcock [9] classified time-series land cover maps from Landsat datasets (1982–2011) in coastal New England in the United States, achieving an OA of approximately 90%. Viana et al. [66] classified LULC maps with time-series Landsat datasets from 1995 to 2015 with 221 Landsat images in the municipality of Beja in the Alentejo region of Portugal, providing an OA of 76%. Franklin et al. [67] classified land cover with time-series Landsat datasets (1990–2010) in the Boreal Mixedwood Region of Northern Ontario, Canada, providing an OA of approximately 87.98%. Utilizing all available Landsat images (2011–2015) of Melbourne, Sao Paulo, Hamburg, and Chicago, Zhang et al. [68] quantified the changes of seasons in different urban land cover types; the overall accuracy percentage was higher than 86%, and the Kappa hat coefficient was greater than 0.80.

### *4.3. Time-Series LST Estimation, Simulation, and Reconstruction*

The time-series LST reconstruction through LST estimation using the SC method and LST simulation using the HA model is a semi-automatic process performed that can provide an acceptable result. Nevertheless, there are some limitations concerning this approach. Firstly, images with a high temporal frequency are needed to guarantee the accuracy of the result by this method. Therefore, a large amount of data storage space and long processing times are required. Secondly, the SC algorithm is a widely used LST inversion algorithm [69–72] that provides RMSEs of around 1.5 K when water vapor content is less than 3 g/cm$^2$. However, the SC algorithm provides RMSEs higher than 5 K when water vapor content is greater than 3 g/cm$^2$ [50,51]. Therefore, when the water vapor content of a pixel (which may be a non-contaminated pixel) is greater than 3 g/cm$^2$, the estimated LST of this pixel will be replaced by the simulated LST. It may ignore some valuable LST extreme points.

### 4.4. Impact of LULC Change on LST

The LULC change on LST shows that the average LST, annual LST change in urban areas are higher than those in other non-urban areas. Rapid urbanization across many regions globally is altering the existing LULC, which is significantly raising the LST.

The impact of LULC change on LST in this study is comparable with other scholars' studies. Fu and Weng [45] analyzed the impact of time-series LULC change on LST with Landsat imagery using decomposition analysis in the metropolitan area of Atlanta. Their study revealed a difference of 1.8 K per decade in the trend component between urban and other land cover types. Meanwhile, the most considerable difference in annual LST variation (5.7 K) and the most significant difference in the trend component (0.146 K/year) were generated when evergreen forest was converted to medium-intensity urban land. Khamchiangta and Dhakal [73] performed the time-series analysis of LULC characteristics and its relationships with the intensity of the urban heat island (UHI) in the Bangkok metropolitan area. The results showed that the built-up area constituted approximately 30% of the total area in 1991 and this sharply increased to approximately 55% in 2016. UHI intensity continually rose from 11.91 °C to 16.21 °C between 1991 and 2016, resulting in a nearly 5 °C increase in Bangkok.

### 4.5. Semi-Automatic Process for Multitemporal LULC Classification and LST Reconstruction

The semi-automatic process for multitemporal LULC classification and LST reconstruction can be used to better understand the impact of LULC change on LST. However, multitemporal analysis requires many images and long processing times. In this study, time-series estimated LST was first calculated semi-automatically from time-series BT, emissivity, and water vapor content. Then, time-series simulated LST was semi-automatically fit from the time-series estimated LST and time-series indicator. Moreover, time-series reconstructed LST was created semi-automatically from the indicator cube, LULC cube, estimated LST cube, and simulated LST cube. All the processes can be programmed using MATLAB software for quick implementation.

The most time-consuming stage is in Section 2.3.3(2). It took about 60 hours to process the whole study with a 64-core supercomputer (about 1 second to process 1 pixel with one core CPU); therefore, a computer with better performance can save processing time. However, recently, GEE and the Google Cloud Platform (GCP) have emerged as important cloud-based platforms for LULC classification. They can provide a large amount of multi-source satellite data and a high-performance computation service. Zhang et al. [74] proposed using the GEE platform to automatically screen invalid image pixels in Landsat images by generating a polygon smaller than the bounding box of each scene. Xie et al. [75] proposed a method for automating land cover classification by adopting time-series Landsat data on the GEE platform. Stromann et al. [76] explored dimensionality reduction and feature selection for land cover classification with time-series Sentinel data using GEE and GCP.

### 4.6. Limitations of LST Reconstruction

The QA band is very important for detecting the contaminated pixels because the LST of these contaminated pixels will be incorrectly estimated. Therefore, these incorrectly estimated LST values will be replaced by simulated LST for LST reconstruction, as we have discussed in the previous sections. However, sometimes, the QA band cannot detect all the contaminated pixels. Figure 18 shows a zoom-in view of the northeastern area of the city, which is obtained using the mask of Figures 7a and 12a. It can be clearly seen that the LST in a narrow "border" is still underestimated since the contaminated pixels at the edge are not recognized by the QA band. In future work, it is better to expand the range of contaminated pixels, which are identified based on the QA band, by a few pixels to avoid remaining unidentified contaminated pixels. Laraby, et al. [77] pointed out that the error in determining the LST also depends on the distance from the cloud. In future work, it is necessary to establish the relationship between cloud proximity and estimated LST errors, and provide the user with a per-pixel map of estimated LST errors. Afterwards, these estimated LST with higher errors should also be replaced with the simulated LST.

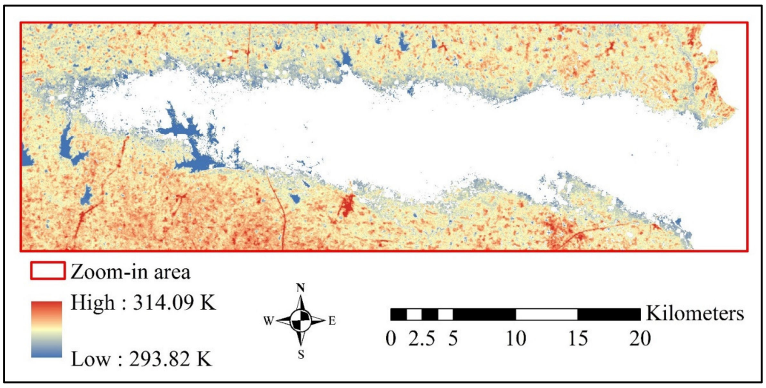


**Figure 18.** A zoom-in area of the estimated LST where is masked by the QA band.

## 5. Conclusions

In this study, the time-series land surface temperature (LST) dataset, which was firstly estimated using the single-channel (SC) algorithm and was reconstructed to minimize errors using harmonic analysis (HA), was successfully established to study the impact of land use and land cover (LULC) change on LST due to urbanization. The average overall accuracy and Kappa hat coefficients of the LULC maps of the four selected years (2001, 2006, 2014, and 2020) using harmonic analysis with a minimum spectral distance algorithm were higher than 90% and 80%, respectively. In these four years, the average producer accuracy and user accuracy from different LULC types were also more than 85%. For time-series LST dataset verification, the mean error value between the simulated LST using HA and the estimated LST using the SC method was 0.03 K. Meanwhile, the mean absolute error was 1.54 K. In addition, the study of multitemporal LULC change on LST using spatial and decomposition analyses confirmed that when agricultural land, forest land, and water bodies were converted into urban and built-up land, the LST difference of urban and non-urban areas, LST, increasing speed of LST, and annual LST change would increase as expected. Thus, it can be reconfirmed that, in Hefei City, land use and land cover changes due to urbanization impact the land surface temperature. Consequently, in rapidly expanding cities, a mitigation plan to reduce LST should be prepared by the corresponding agencies, such as the Meteorological Bureau, Planning and Natural Resources Bureau, and Ecological Environment Bureau.

**Author Contributions:** Conceptualization, J.S. and S.O.; methodology, J.S. and S.O.; software, J.S.; validation, J.S. and S.O.; formal analysis, J.S.; investigation, J.S.; resources, J.S.; data curation, J.S.; writing—original draft preparation, J.S.; writing—review and editing, S.O.; visualization, J.S.; supervision, S.O.; project administration, J.S.; funding acquisition, J.S. All authors have read and agreed to the published version of the manuscript.

**Funding:** This research was funded by the Natural Science Research Project of the Anhui Education Department, Grant Number KJ2019A0707.

**Institutional Review Board Statement:** Not applicable.

**Informed Consent Statement:** Not applicable.

**Data Availability Statement:** Not applicable.

**Acknowledgments:** The facility support from Tongling University is gratefully acknowledged by the authors. The authors also thank the anonymous reviewers for their valuable comments and suggestions, which improved our manuscript from various perspectives.

**Conflicts of Interest:** The authors declare no conflict of interest.

## References

1. Arnfield, A.J. Two decades of urban climate research: A review of turbulence, exchanges of energy and water, and the urban heat island. *Int. J. Climatol.* **2003**, *23*, 1–26. [CrossRef]
2. Bastiaanssen, W.G.M.; Menenti, M.; Feddes, R.A.; Holtslag, A.A.M. A remote sensing surface energy balance algorithm for land (SEBAL). 1. Formulation. *J. Hydrol.* **1998**, *212–213*, 198–212. [CrossRef]
3. Hansen, J.; Ruedy, R.; Sato, M.; Lo, K. Global surface temperature change. *Rev. Geophys.* **2010**, *48*, RG4004. [CrossRef]
4. Kogan, F.N. Operational space technology for global vegetation assessment. *Bull. Am. Meteorol. Soc.* **2001**, *82*, 1949–1964. [CrossRef]
5. Su, Z. The Surface Energy Balance System (SEBS) for estimation of turbulent heat fluxes. *Hydrol. Earth Syst. Sci.* **2002**, *6*, 85–99. [CrossRef]
6. Voogt, J.A.; Oke, T.R. Thermal remote sensing of urban climates. *Remote Sens. Environ.* **2003**, *86*, 370–384. [CrossRef]
7. Weng, Q. Thermal infrared remote sensing for urban climate and environmental studies: Methods, applications, and trends. *ISPRS J. Photogramm. Remote Sens.* **2009**, *64*, 335–344. [CrossRef]
8. Weng, Q.; Lu, D.; Schubring, J. Estimation of land surface temperature–vegetation abundance relationship for urban heat island studies. *Remote Sens. Environ.* **2004**, *89*, 467–483. [CrossRef]
9. Zhu, Z.; Woodcock, C.E. Continuous change detection and classification of land cover using all available Landsat data. *Remote Sens. Environ.* **2014**, *144*, 152–171. [CrossRef]
10. Bonan, G.B.; Pollard, D.; Thompson, S.L. Effects of boreal forest vegetation on global climate. *Nature* **1992**, *359*, 716. [CrossRef]
11. Foley, J.A.; DeFries, R.; Asner, G.P.; Barford, C.; Bonan, G.; Carpenter, S.R.; Chapin, F.S.; Coe, M.T.; Daily, G.C.; Gibbs, H.K.; et al. Global Consequences of Land Use. *Science* **2005**, *309*, 570–574. [CrossRef]
12. Lee, E.; He, Y.; Zhou, M.; Liang, J. Potential feedback of recent vegetation changes on summer rainfall in the Sahel. *Phys. Geogr.* **2015**, *36*, 449–470. [CrossRef]
13. Mahmood, R.; Pielke, R.A.; Hubbard, K.G.; Niyogi, D.; Dirmeyer, P.A.; McAlpine, C.; Carleton, A.M.; Hale, R.; Gameda, S.; Beltrán-Przekurat, A.; et al. Land cover changes and their biogeophysical effects on climate. *Int. J. Climatol.* **2014**, *34*, 929–953. [CrossRef]
14. Pielke, R.A. Land Use and Climate Change. *Science* **2005**, *310*, 1625–1626. [CrossRef]
15. McPherson, R.A. A review of vegetation—Atmosphere interactions and their influences on mesoscale phenomena. *Prog. Phys. Geogr.* **2007**, *31*, 261–285. [CrossRef]
16. Qiao, Z.; Tian, G.; Zhang, L.; Xu, X. Influences of Urban Expansion on Urban Heat Island in Beijing during 1989–2010. *Adv. Meteorol.* **2014**, *2014*, 187169. [CrossRef]
17. Ongsomwang, S.; Dasananda, S.; Prasomsup, W. Spatio-temporal urban heat island phenomena assessment using landsat imagery: A case study of Bangkok metropolitan and its Vicinity, Thailand. *Environ. Nat. Resour. J.* **2018**, *16*, 29–44. [CrossRef]
18. Srivanit, M.; Hokao, K.; Phonekeo, V. Assessing the Impact of Urbanization on Urban Thermal Environment: A Case Study of Bangkok Metropolitan. *Int. J. Appl. Sci. Technol.* **2012**, *2*, 243–256.
19. Fonseka, H.P.U.; Zhang, H.; Sun, Y.; Su, H.; Lin, H.; Lin, Y. Urbanization and Its Impacts on Land Surface Temperature in Colombo Metropolitan Area, Sri Lanka, from 1988 to 2016. *Remote Sens.* **2019**, *11*, 957. [CrossRef]
20. Li, F.; Sun, W.; Yang, G.; Weng, Q. Investigating Spatiotemporal Patterns of Surface Urban Heat Islands in the Hangzhou Metropolitan Area, China, 2000–2015. *Remote Sens.* **2019**, *11*, 1553. [CrossRef]
21. Simwanda, M.; Ranagalage, M.; Estoque, R.C.; Murayama, Y. Spatial Analysis of Surface Urban Heat Islands in Four Rapidly Growing African Cities. *Remote Sens.* **2019**, *11*, 1645. [CrossRef]
22. Qiao, Z.; Liu, L.; Qin, Y.; Xu, X.; Wang, B.; Liu, Z. The Impact of Urban Renewal on Land Surface Temperature Changes: A Case Study in the Main City of Guangzhou, China. *Remote Sens.* **2020**, *12*, 794. [CrossRef]
23. Dang, T.; Yue, P.; Bachofer, F.; Wang, M.; Zhang, M. Monitoring Land Surface Temperature Change with Landsat Images during Dry Seasons in Bac Binh, Vietnam. *Remote Sens.* **2020**, *12*, 4067. [CrossRef]
24. Xu, J.; Zhao, Y.; Sun, C.; Liang, H.; Yang, J.; Zhong, K.; Li, Y.; Liu, X. Exploring the Variation Trend of Urban Expansion, Land Surface Temperature, and Ecological Quality and Their Interrelationships in Guangzhou, China, from 1987 to 2019. *Remote Sens.* **2021**, *13*, 1019. [CrossRef]
25. Shen, Z.; Xu, X. Influence of the Economic Efficiency of Built-Up Land (EEBL) on Urban Heat Islands (UHIs) in the Yangtze River Delta Urban Agglomeration (YRDUA). *Remote Sens.* **2020**, *12*, 3944. [CrossRef]
26. Wang, R.; Hou, H.; Murayama, Y.; Derdouri, A. Spatiotemporal Analysis of Land Use/Cover Patterns and Their Relationship with Land Surface Temperature in Nanjing, China. *Remote Sens.* **2020**, *12*, 440. [CrossRef]
27. Athukorala, D.; Murayama, Y. Urban Heat Island Formation in Greater Cairo: Spatio-Temporal Analysis of Daytime and Nighttime Land Surface Temperatures along the Urban–Rural Gradient. *Remote Sens.* **2021**, *13*, 1396. [CrossRef]

28. Liu, F.; Hou, H.; Murayama, Y. Spatial Interconnections of Land Surface Temperatures with Land Cover/Use: A Case Study of Tokyo. *Remote Sens.* **2021**, *13*, 610. [CrossRef]
29. Mohamed, M.; Othman, A.; Abotalib, A.Z.; Majrashi, A. Urban Heat Island Effects on Megacities in Desert Environments Using Spatial Network Analysis and Remote Sensing Data: A Case Study from Western Saudi Arabia. *Remote Sens.* **2021**, *13*, 1941. [CrossRef]
30. Singh, P.; Kikon, N.; Verma, P. Impact of land use change and urbanization on urban heat island in Lucknow city, Central India. A remote sensing based estimate. *Sustain. Cities Soc.* **2017**, *32*, 100–114. [CrossRef]
31. Tran, H.; Uchihama, D.; Ochi, S.; Yasuoka, Y. Assessment with satellite data of the urban heat island effects in Asian mega cities. *Int. J. Appl. Earth Obs. Geoinf.* **2006**, *8*, 34–48. [CrossRef]
32. Kikon, N.; Singh, P.; Singh, S.K.; Vyas, A. Assessment of urban heat islands (UHI) of Noida City, India using multi-temporal satellite data. *Sustain. Cities Soc.* **2016**, *22*, 19–28. [CrossRef]
33. Estoque, R.C.; Murayama, Y.; Myint, S.W. Effects of landscape composition and pattern on land surface temperature: An urban heat island study in the megacities of Southeast Asia. *Sci. Total Environ.* **2017**, *577*, 349–359. [CrossRef] [PubMed]
34. Fang, G. Prediction and analysis of urban heat island effect in dangshan by remote sensing. *Int. J. Smart Sens. Intell. Syst.* **2015**, *8*, 2195–2211. [CrossRef]
35. Xu, Y.; Shen, Y. Reconstruction of the land surface temperature time series using harmonic analysis. *Comput. Geosci.* **2013**, *61*, 126–132. [CrossRef]
36. Weng, Q.; Fu, P.; Gao, F. Generating daily land surface temperature at Landsat resolution by fusing Landsat and MODIS data. *Remote Sens. Environ.* **2014**, *145*, 55–67. [CrossRef]
37. Neteler, M. Estimating Daily Land Surface Temperatures in Mountainous Environments by Reconstructed MODIS LST Data. *Remote Sens.* **2010**, *2*, 333–351. [CrossRef]
38. Ke, L.; Ding, X.; Song, C. Reconstruction of Time-Series MODIS LST in Central Qinghai-Tibet Plateau Using Geostatistical Approach. *IEEE Geosci. Remote Sens. Lett.* **2013**, *10*, 1602–1606. [CrossRef]
39. Kang, J.; Tan, J.; Jin, R.; Li, X.; Zhang, Y. Reconstruction of MODIS Land Surface Temperature Products Based on Multi-Temporal Information. *Remote Sens.* **2018**, *10*, 1112. [CrossRef]
40. Shang, H.; Jia, L.; Menenti, M. Analyzing the Inundation Pattern of the Poyang Lake Floodplain by Passive Microwave Data. *J. Hydrometeorol.* **2015**, *16*, 652–667. [CrossRef]
41. Menenti, M.; Malamiri, H.R.G.; Shang, H.; Alfieri, S.M.; Maffei, C.; Jia, L. *Observing the Response of Terrestrial Vegetation to Climate Variability across a Range of Time Scales by Time Series Analysis of Land Surface Temperature*; Springer: Heidelberg, Germany, 2016; p. 447.
42. Sun, J.; Ongsomwang, S. Multitemporal Land Use and Land Cover Classification from Time-Series Landsat Datasets Using Harmonic Analysis with a Minimum Spectral Distance Algorithm. *ISPRS Int. J. Geo-Inf.* **2020**, *9*, 67. [CrossRef]
43. Lo, C.P.; Quattrochi, D.A. Land Use and Land Cover Change, Urban Heat Island Phenomenon, and Health Implications: A Remote Sensing Approach. *Photogramm. Eng. Remote Sens.* **2003**, *69*, 1053–1063. [CrossRef]
44. Statistics Bureau of Anhui Province. Anhui Statistical Yearbook. Available online: http://tjj.ah.gov.cn/ssah/qwfbjd/tjnj/index.html (accessed on 25 February 2021).
45. Fu, P.; Weng, Q. A time series analysis of urbanization induced land use and land cover change and its impact on land surface temperature with Landsat imagery. *Remote Sens. Environ.* **2016**, *175*, 205–214. [CrossRef]
46. USGS. *Landsat QA Tools User Guide*; Department of the Interior, U.S. Geological Survey: Reston, VA, USA, 2017; p. 33.
47. Vicente-Serrano, S.M.; Pérez-Cabello, F.; Lasanta, T. Assessment of radiometric correction techniques in analyzing vegetation variability and change using time series of Landsat images. *Remote Sens. Environ.* **2008**, *112*, 3916–3934. [CrossRef]
48. USGS. *Landsat 4–7 Surface Reflectance (LEDAPS) Product Guide*; Department of the Interior, U.S. Geological Survey: Reston, VA, USA, 2019; p. 38.
49. USGS. *Landsat 8 Surface Reflectance Code(LaSRC) Product Guide*; Department of the Interior, U.S. Geological Survey: Reston, VA, USA, 2019; p. 39.
50. Jiménez-Muñoz, J.C.; Cristobal, J.; Sobrino, J.A.; Soria, G.; Ninyerola, M.; Pons, X. Revision of the Single-Channel Algorithm for Land Surface Temperature Retrieval from Landsat Thermal-Infrared Data. *IEEE Trans. Geosci. Remote Sens.* **2009**, *47*, 339–349. [CrossRef]
51. Jiménez-Muñoz, J.C.; Sobrino, J.A.; Skoković, D.; Mattar, C.; Cristóbal, J. Land Surface Temperature Retrieval Methods from Landsat-8 Thermal Infrared Sensor Data. *IEEE Geosci. Remote Sens. Lett.* **2014**, *11*, 1840–1843. [CrossRef]
52. Sobrino, J.A.; Jiménez-Muñoz, J.C.; Soria, G.; Romaguera, M.; Moreno, L.G.A.-J.; Plaza, A.; Martinez, P. Land Surface Emissivity Retrieval From Different VNIR and TIR Sensors. *IEEE Trans. Geosci. Remote Sens.* **2008**, *46*, 316–327. [CrossRef]
53. Sobrino, J.A.; Jiménez-Muñoz, J.C.; Paolini, L. Land surface temperature retrieval from LANDSAT TM 5. *Remote Sens. Environ.* **2004**, *90*, 434–440. [CrossRef]
54. Jet Propulsion Laboratory. ECOSTRESS Spectral Library. Available online: https://speclib.jpl.nasa.gov/ (accessed on 25 February 2021).
55. Li, Z.; Tang, B.; Wu, H.; Ren, H.; Yan, G.; Wan, Z.; Trigo, I.F.; Sobrino, J.A. Satellite-derived land surface temperature: Current status and perspectives. *Remote Sens. Environ.* **2013**, *131*, 14–37. [CrossRef]

56. Gao, B.-C.; Kaufman, Y.J. Water vapor retrievals using Moderate Resolution Imaging Spectroradiometer (MODIS) near-infrared channels. *J. Geophys. Res. Atmos.* **2003**, *108*. [CrossRef]
57. Congalton, R.G.; Green, K. *Assessing the Accuracy of Remotely Sensed Data—Principles and Practices*, 2nd ed.; CRC Press, Taylor & Francis Group: Boca Raton, NW, USA, 2009; p. 210.
58. Tortora, R.D. A Note on Sample Size Estimation for Multinomial Populations. *Am. Stat.* **1978**, *32*, 100–102. [CrossRef]
59. Jensen, J.R. *Introductory Digital Image Processing: A Remote Sensing Perspective*; Prentice Hall Press: Upper Saddle River, NJ, USA, 2015; p. 659.
60. Cort, J.W.; Kenji, M. Advantages of the mean absolute error (MAE) over the root mean square error (RMSE) in assessing average model performance. *Clim. Res.* **2005**, *30*, 79–82. [CrossRef]
61. Nijbroek, R.; Piikki, K.; Söderström, M.; Kempen, B.; Turner, K.G.; Hengari, S.; Mutua, J. Soil Organic Carbon Baselines for Land Degradation Neutrality: Map Accuracy and Cost Tradeoffs with Respect to Complexity in Otjozondjupa, Namibia. *Sustainability* **2018**, *10*, 1610. [CrossRef]
62. Story, M.; Congalton, R.G. Accuracy Assessment: A User's Perspective. *Photogramm. Eng. Remote Sens.* **1986**, *52*, 397–399.
63. Anderson, J.R.; Hardy, E.E.; Roach, J.T.; Witmer, R.E. A Land Use and Land Cover Classification System for Use with Remote Sensor Data. United States Government Printing Office: Washington, DC, USA, 1976; p. 34.
64. Landis, J.R.; Koch, G.G. The Measurement of Observer Agreement for Categorical Data. *Biometrics* **1977**, *33*, 159–174. [CrossRef] [PubMed]
65. Calderón-Loor, M.; Hadjikakou, M.; Bryan, B.A. High-resolution wall-to-wall land-cover mapping and land change assessment for Australia from 1985 to 2015. *Remote Sens. Environ.* **2021**, *252*, 112148. [CrossRef]
66. Viana, C.M.; Girão, I.; Rocha, J. Long-Term Satellite Image Time-Series for Land Use/Land Cover Change Detection Using Refined Open Source Data in a Rural Region. *Remote Sens.* **2019**, *11*, 1104. [CrossRef]
67. Franklin, S.E.; Ahmed, O.S.; Wulder, M.A.; White, J.C.; Hermosilla, T.; Coops, N.C. Large Area Mapping of Annual Land Cover Dynamics Using Multitemporal Change Detection and Classification of Landsat Time Series Data. *Can. J. Remote Sens.* **2015**, *41*, 293–314. [CrossRef]
68. Zhang, H.; Wang, T.; Zhang, Y.; Dai, Y.; Jia, J.; Yu, C.; Li, G.; Lin, Y.; Lin, H.; Cao, Y. Quantifying Short-Term Urban Land Cover Change with Time Series Landsat Data: A Comparison of Four Different Cities. *Sensors* **2018**, *18*, 4319. [CrossRef]
69. Chatterjee, R.S.; Singh, N.; Thapa, S.; Sharma, D.; Kumar, D. Retrieval of land surface temperature (LST) from landsat TM6 and TIRS data by single channel radiative transfer algorithm using satellite and ground-based inputs. *Int. J. Appl. Earth Obs. Geoinf.* **2017**, *58*, 264–277. [CrossRef]
70. Duan, S.-B.; Li, Z.-L.; Wang, C.; Zhang, S.; Tang, B.-H.; Leng, P.; Gao, M.-F. Land-surface temperature retrieval from Landsat 8 single-channel thermal infrared data in combination with NCEP reanalysis data and ASTER GED product. *Int. J. Remote Sens.* **2019**, *40*, 1763–1778. [CrossRef]
71. Walawender, J.P.; Szymanowski, M.; Hajto, M.J.; Bokwa, A. Land Surface Temperature Patterns in the Urban Agglomeration of Krakow (Poland) Derived from Landsat-7/ETM+ Data. *Pure Appl. Geophys.* **2014**, *171*, 913–940. [CrossRef]
72. Orhan, O.; Ekercin, S.; Dadaser-Celik, F. Use of Landsat Land Surface Temperature and Vegetation Indices for Monitoring Drought in the Salt Lake Basin Area, Turkey. *Sci. World J.* **2014**, *2014*, 142939. [CrossRef]
73. Khamchiangta, D.; Dhakal, S. Time series analysis of land use and land cover changes related to urban heat island intensity: Case of Bangkok Metropolitan Area in Thailand. *J. Urban Manag.* **2020**, *9*, 383–395. [CrossRef]
74. Zhang, Q.; Chen, K.; Jing, Q.; Chen, X. Automatic invalid Landsat image pixel screening on the Google Earth engine platform. In Proceedings of the 2016 IEEE International Geoscience and Remote Sensing Symposium (IGARSS), Beijing, China, 10–15 July 2016; pp. 2384–2387.
75. Xie, S.; Liu, L.; Zhang, X.; Yang, J.; Chen, X.; Gao, Y. Automatic Land-Cover Mapping using Landsat Time-Series Data based on Google Earth Engine. *Remote Sens.* **2019**, *11*, 3023. [CrossRef]
76. Stromann, O.; Nascetti, A.; Yousif, O.; Ban, Y. Dimensionality Reduction and Feature Selection for Object-Based Land Cover Classification based on Sentinel-1 and Sentinel-2 Time Series Using Google Earth Engine. *Remote Sens.* **2020**, *12*, 76. [CrossRef]
77. Laraby, K.; Schott, J.; Raqueno, N. *Developing a Confidence Metric for the Landsat Land Surface Temperature Product*; SPIE: Bellingham, WA, USA, 2016; Volume 9840.